

# **Analysis of a Semi-Implicit Algorithm for Low-Frequency Two-Fluid Plasma Modeling**

**December 4, 2009**

C. R. Sovinec,<sup>1</sup> J. R. King,<sup>2</sup> and the NIMROD Team

<sup>1</sup>*University of Wisconsin-Madison, Department of Engineering Physics*

<sup>2</sup>*University of Wisconsin-Madison, Department of Physics*

Prepared for submission to the Journal of Computational Physics

## NOTICE

This report was prepared as an account of work sponsored by the United States Government. Neither the United States nor the United States Department of Energy, nor any of their employees, nor any of their contractors, subcontractors, or their employees, makes any warranty, expressed or implied, or assumes any legal liability or responsibility for the accuracy, completeness, or usefulness of any information, apparatus, product or process disclosed or represents that its use would not infringe privately owned rights.

## Analysis of a Semi-Implicit Algorithm for Low-Frequency Two-Fluid Plasma Modeling

C. R. Sovinec, J. R. King, and the NIMROD Team

### ABSTRACT

A temporally staggered algorithm for advancing solutions of the two-fluid plasma model is analyzed with von Neumann's method and with differential approximation. The implicit leapfrog algorithm [C. R. Sovinec, *et al.*, J. Phys.: Conf. Series 16 (2005) 25-34] is found to be numerically stable at arbitrarily large time-step when the advective, Hall, and gyroviscous terms are temporally centered in their respective advances and the coefficient of the semi-implicit operator meets the criterion found for basic hyperbolic systems. Numerical instability with forward or backward differencing of advection is evident as an ill-posed equation in the differential approximation for a simplified system. At large time-step, the accuracy of the algorithm is comparable to that of the Crank-Nicolson method for all plane waves except the parallel mode that is sensitive to the ion cyclotron resonance. An implementation reproduces theoretical results on the transition from resistive magnetohydrodynamics to two-fluid reconnection in a sheared-slab linear tearing mode. A nonlinear three-dimensional computation in toroidal geometry shows an increasing exponentiation rate of kinetic energy as magnetic reconnection from an internal kink mode changes from current-sheet to 'X-point' geometry.

### 1. INTRODUCTION

Magnetohydrodynamics (MHD) is a useful starting point for studying the macroscopic stability of magnetized plasma. Linear MHD calculations are used routinely to assess the free energy of particular configurations, and nonlinear simulations provide insight into the consequences of instability, such as dynamo effects, relaxation, and partial or complete loss of stored thermal energy. However, the MHD model is very limited as a description of plasma dynamics. It misses drift effects that are important for low-frequency dynamics when particle gyro-orbits are not negligible [1]. In addition, macroscopic relaxation requires magnetic topology change resulting from reconnection, and non-MHD electron dynamics release the magnetic evolution from spatial scales associated with ions, thereby allowing fast reconnection [2-4]. Comprehensive simulation of macroscopic plasma dynamics therefore requires these 'two-fluid' effects, plus kinetic effects for conditions with infrequent collisions.

The differences between the two-fluid and MHD models that lead to new physical effects are also significant from the computational perspective. Electron dynamics and ion magnetization represented by gyroviscosity lead to dispersive normal modes [5-6], where the phase velocity of traveling waves at short-wavelength is faster than that of the long-wavelength modes. For a given level of spatial resolution, a numerical computation with the two-fluid model has a greater range of time-scales than a comparable MHD computation, and the increased stiffness makes implicit methods yet more important. In addition, drift effects impose a preferred direction of propagation for each species, so macroscopic dynamics tend to have complex frequencies. As a result, implicit methods for advancing the system of equations typically have matrices that are not Hermitian, even when the matrices for comparable MHD algorithms are.

Several efforts [7-10] are investigating the time-centered Crank-Nicolson implicit method [11] method for fluid-based plasma models. Fully centered and other methods [12] with implicit

nonlinear terms use Newton-Raphson iteration. There have been significant advances with the advent of ‘matrix-free’ methods [13], where elements of the Jacobi matrix are not required if the linear systems are solved with Krylov-based iteration. Like most practical applications of iterative Krylov methods, preconditioning is essential, and an approximation of the Jacobi matrix is needed in this case. Whether the theoretical advantage of nonlinear time-centered accuracy can be achieved in practice depends on the quality and efficiency of the approximation. Thus, preconditioning is a focus of active research for these methods [14]. One beneficial aspect of magnetic confinement applications is that nonlinear perturbations in regions of high temperature are much smaller than the background; otherwise, there would be no confinement. Thus, the stiffness from fast waves is largely a linear property.

Semi-implicit algorithms that selectively restrict the propagation of fast normal modes have proven successful for nonlinear multi-scale magnetohydrodynamics [15-18], and extensions for the two-fluid model have been proposed [19-20]. Here, we consider the numerical properties of an ‘implicit leapfrog’ algorithm that staggers flow-velocity in time from the other fields. The leapfrog character here refers to temporal staggering of distinct parts of the system state that are numerically analogous to coordinates and their canonical momenta in computations for a Hamiltonian system. The next state in a temporal sequence only depends on the previous state, so the advance is a two-level scheme. This is in contrast with multi-level leapfrog methods [21], such as midpoint, that may suffer numerical instability [22-23]. A practical advantage of staggering is that it allows an implementation to advance each physical field separately, which reduces the sizes and condition numbers of the matrices required for a given spatial representation. This feature and the semi-implicit operator for the advance of flow velocity are in common with the semi-implicit MHD algorithms [15-18]. However, for numerical stability reasons described in Section 3, advection is handled implicitly for each advance. In addition, the two-fluid Ohm’s law is time-centered during the advance of magnetic field. This is in contrast to the semi-implicit styled magnetic advance that is presented in Ref. [19] and reconsidered below in Appendix A.

The primary findings of our analyses are that the time-staggered semi-implicit method for MHD can be extended to include two-fluid effects when the two-fluid and advective terms are time-centered in the separate advances. The algorithm can be made numerically stable for arbitrarily large time-step values and remains free of numerical dissipation. Dissipative physical effects are represented by resistive dissipation in our analysis, which shows unconditional stability for centered and backward differencing of this term. With centered dissipation, the algorithm is second-order accurate. Tests on plane waves show accuracy that is comparable to the Crank-Nicolson method at large time-step and wavenumber, except for the low-frequency parallel mode that is sensitive to the ion cyclotron resonance. Linear tearing mode benchmarks show that the algorithm accurately reproduces transitions from MHD to two-fluid reconnection with temporal accuracy that is comparable to our resistive MHD computations. An example nonlinear computation demonstrates two-fluid reconnection in toroidal geometry.

Our algorithm is detailed in Section 2 after presenting the two-fluid system of equations. In Section 3, we analyze the numerical stability and accuracy for all plane-wave polarizations of the model using von Neumann’s method. For the general case, the resulting dispersion relation is evaluated numerically. Insight on the effects of centering parameters for advection and diffusion is developed with the method of differential approximation [24-26], also known as modified equation analysis [27-28]. Benchmarking on two-fluid linear tearing modes and the example

three-dimensional nonlinear application are presented in Section 4. Conclusions from the analysis and applications are drawn in Section 5.

## 2. SYSTEM OF EQUATIONS AND ALGORITHM

All fluid-based models for high-temperature plasma are approximations. Closure of fluid equations is usually based on dynamical spatial scales being much larger than the effective mean-free-path for particle scattering through collisions, and that condition is violated in most magnetic confinement experiments. In addition, the most common Braginskii form of the two-fluid equations [29] is derived with the assumption that flow speeds are of the order of the ion thermal speed. Further assuming low frequency, such that quasineutrality ( $n \equiv n_e \equiv n_i$ ) is satisfied and that displacement current is negligible, and neglecting the electron thermal force, we arrive at the system considered here:

$$\frac{\partial n}{\partial t} + \nabla \cdot (n\mathbf{V}) = 0 \quad (1)$$

$$mn \left( \frac{\partial}{\partial t} + \mathbf{V} \cdot \nabla \right) \mathbf{V} = \mathbf{J} \times \mathbf{B} - \nabla p - \nabla \cdot \underline{\Pi} \quad (2)$$

$$\frac{3}{2} n \left( \frac{\partial}{\partial t} + \mathbf{V}_\alpha \cdot \nabla \right) T_\alpha = -n T_\alpha \nabla \cdot \mathbf{V}_\alpha - \nabla \cdot \mathbf{q}_\alpha + Q_\alpha \quad (3)$$

$$\frac{\partial \mathbf{B}}{\partial t} = -\nabla \times \left[ \eta \mathbf{J} - \mathbf{V} \times \mathbf{B} + \frac{1}{ne} \mathbf{J} \times \mathbf{B} - \frac{T_e}{ne} \nabla n + \frac{m_e}{ne^2} \frac{\partial}{\partial t} \mathbf{J} \right] \quad (4)$$

$$\mu_0 \mathbf{J} = \nabla \times \mathbf{B} \quad (5)$$

$$\nabla \cdot \mathbf{B} = 0 \quad (6)$$

where  $\mathbf{V}$  is the center-of-mass flow velocity (essentially the ion flow velocity, since electron inertia is small for low-frequency dynamics, and the effective mass  $m$  is approximately the ion mass  $m_i$ ). The magnetic induction  $\mathbf{B}$  and charge-current density  $\mathbf{J}$  are related by the low-frequency Ampere's law, Eq. (5). The system allows for separate electron and ion temperatures ( $T_\alpha$ ,  $\alpha=i,e$ ) with conductive heat-flux vectors  $\mathbf{q}_\alpha$  and sources  $Q_\alpha$  and the pressure in the flow evolution equation (2) is the sum of the electron and ion contributions,  $p = n(T_i + T_e)$  with temperature in units of energy. Drag between electron and ion flows is represented by the electrical resistivity ( $\eta$ ), and the stress tensor  $\underline{\Pi}$  is a function of flow-velocity gradients.

The most important two-fluid effects for low-frequency dynamics result from the Hall term,  $\mathbf{J} \times \mathbf{B}/ne$  that is part of the electric field relation in the right side of Eq. (4) and from the gyroviscous stress that is part of  $\underline{\Pi}$ . The latter can be expressed as

$$\underline{\Pi}_{gv} = \frac{nT_i}{4\Omega_i} \left[ \hat{\mathbf{b}} \times \underline{\mathbf{W}} \cdot (\underline{\mathbf{I}} + 3\hat{\mathbf{b}}\hat{\mathbf{b}}) - (\underline{\mathbf{I}} + 3\hat{\mathbf{b}}\hat{\mathbf{b}}) \cdot \underline{\mathbf{W}} \times \hat{\mathbf{b}} \right], \quad (7)$$

where  $\Omega_i = eB/m_i$  is the ion cyclotron frequency,  $\hat{\mathbf{b}} = \mathbf{B}/B$ ,  $\underline{\mathbf{I}}$  is the identity tensor, and  $\underline{\mathbf{W}}$  is the traceless rate-of-strain tensor

$$\underline{\mathbf{W}} = \nabla \mathbf{V} + \nabla \mathbf{V}^T - \frac{2}{3} \underline{\mathbf{I}} \nabla \cdot \mathbf{V} . \quad (8)$$

More realistic orderings for the nonlinear dynamics of interest have thermal speeds larger than the flow speeds [1], which introduces additional stresses that are associated with heat flows [30]. The simpler system considered here is, nonetheless, a starting point for addressing nonlinear two-fluid dynamics and includes the most significant effects on stiffness for numerical algorithms. In the same spirit, the last term in (4) represents part of the electron inertia effects in Ohm's law. This term and the missing advective part, which scales as  $kV/\omega$  relative to this term (where  $k$  and  $\omega$  are wavenumber and frequency, respectively), may be quantitatively important for magnetic reconnection, depending on collisionality and the rate of reconnection.

Our temporal algorithm for solving initial-value computations with Eqs. (1-7) has been presented in Refs. [6, 20]. Similar to our MHD algorithm [17], the semi-discrete equations have  $\mathbf{V}$  defined at integer time levels and  $\mathbf{B}$ ,  $n$ , and  $T_\alpha$  defined at half-integer levels:

$$\begin{aligned} mn^{j+1/2} \left( \frac{\Delta \mathbf{V}}{\Delta t} + \frac{1}{2} \mathbf{V}^j \cdot \nabla \Delta \mathbf{V} + \frac{1}{2} \Delta \mathbf{V} \cdot \nabla \mathbf{V}^j + \frac{1}{4} \Delta \mathbf{V} \cdot \nabla \Delta \mathbf{V} \right) - \\ \Delta t \underline{\mathbf{L}}^{j+1/2} (\Delta \mathbf{V}) + \nabla \cdot \underline{\mathbf{\Pi}}^{j+1/2} (\Delta \mathbf{V}) = \mathbf{J}^{j+1/2} \times \mathbf{B}^{j+1/2} \\ - mn^{j+1/2} \mathbf{V}^j \cdot \nabla \mathbf{V}^j - \nabla p^{j+1/2} - \nabla \cdot \underline{\mathbf{\Pi}}^{j+1/2} (\mathbf{V}^j) \end{aligned} \quad (9)$$

$$\frac{\Delta n}{\Delta t} + \frac{1}{2} \nabla \cdot (\mathbf{V}^{j+1} \Delta n) = -\nabla \cdot (\mathbf{V}^{j+1} n^{j+1/2}) \quad (10)$$

$$\begin{aligned} \frac{3\bar{n}}{2} \left( \frac{\Delta T_\alpha}{\Delta t} + \frac{1}{2} \mathbf{V}_\alpha^{j+1} \cdot \nabla \Delta T_\alpha \right) + \frac{1}{2} \bar{n} \Delta T_\alpha \nabla \cdot \mathbf{V}_\alpha^{j+1} + \frac{1}{2} \nabla \cdot [\mathbf{q}_\alpha (\Delta T_\alpha)] = \\ - \frac{3\bar{n}}{2} \mathbf{V}_\alpha^{j+1} \cdot \nabla T_\alpha^{j+1/2} - \bar{n} T_\alpha^{j+1/2} \nabla \cdot \mathbf{V}_\alpha^{j+1} \\ - \nabla \cdot [\mathbf{q}_\alpha (T_\alpha^{j+1/2})] + Q_\alpha^{j+1/2} \end{aligned} \quad (11)$$

$$\begin{aligned} \frac{\Delta \mathbf{B}}{\Delta t} + \nabla \times \left( \frac{m_e}{\mu_0 \bar{n} e^2} \nabla \times \frac{\Delta \mathbf{B}}{\Delta t} \right) - \frac{1}{2} \nabla \times (\mathbf{V}^{j+1} \times \Delta \mathbf{B}) \\ + \frac{1}{2} \nabla \times \frac{1}{\bar{n} e} \left( \mathbf{J}^{j+1/2} \times \Delta \mathbf{B} + \Delta \mathbf{J} \times \mathbf{B}^{j+1/2} + \frac{1}{2} \Delta \mathbf{J} \times \Delta \mathbf{B} \right) + \frac{1}{2} \nabla \times \eta \Delta \mathbf{J} = \\ - \nabla \times \left[ \frac{1}{\bar{n} e} \left( \mathbf{J}^{j+1/2} \times \mathbf{B}^{j+1/2} - \bar{T}_e \nabla \bar{n} \right) - \mathbf{V}^{j+1} \times \mathbf{B}^{j+1/2} + \eta \mathbf{J}^{j+1/2} \right] , \end{aligned} \quad (12)$$

where superscripts indicate time-level indices,  $\Delta$  indicates the change over a step, and over-bars indicate the average of the beginning and end of a step. The semi-implicit operator for stabilizing low-frequency waves is the same used for MHD,

$$\mathbf{L}(\Delta\mathbf{V}) = C_0 \left\{ \frac{1}{\mu_0} [\nabla \times \nabla \times (\Delta\mathbf{V} \times \mathbf{B})] \times \mathbf{B} + \mathbf{J} \times \nabla \times (\Delta\mathbf{V} \times \mathbf{B}) + \nabla \left( \Delta\mathbf{V} \cdot \nabla p + \frac{5}{3} p \nabla \cdot \Delta\mathbf{V} \right) \right\} + C_1 p_{nl} \nabla^2 \Delta\mathbf{V} \quad , \quad (13)$$

where  $C_0$  is a coefficient for the ideal-MHD force operator, and  $C_1$  is a coefficient for the Laplacian part with  $p_{nl}$  the ‘nonlinear pressure,’ which is typically orders of magnitude smaller than the total pressure, as described in Ref. [17]. Terms in (9-12) are time-centered for each respective advance (including coefficients in operators) by the temporal staggering, by averaging previously advanced fields, and by implicit computation. The only algebraically nonlinear implicit terms are the advective term in (9) and the Hall term in (12). Both are quadratic (in  $\Delta\mathbf{V}$  for one and in  $\Delta\mathbf{B}$  for the other), so Newton iteration is straightforward.

Our focus here is on the properties of the semi-discrete system Eqs. (9-13). Nonetheless, a couple of points regarding its implementation in the NIMROD code are important. First, the implementation uses the implicit diffusive correction,  $\sim \nabla \nabla \cdot \mathbf{B}$ , for magnetic divergence error, as described in Ref. [17]. In addition, numerical smoothing of the particle number density is accomplished with either an artificial Fick’s law term or a hyper-diffusivity,  $\sim \nabla^4 n$  added to Eq. (10). The electron inertia term in Eq. (12) serves important numerical roles, regardless of its physical importance in an application. In the matrix for the advance of  $\mathbf{B}$  that results from spatial discretization, the electron inertia provides a symmetric contribution. Including it provides the  $R$ -mode branch with a resonance at the electron cyclotron frequency, which limits the range of frequencies at sufficiently large wavenumbers. Consequently, this term helps limit the condition number of the matrix for the advance of  $\mathbf{B}$  as spatial resolution is increased, even when the physically correct value of  $m_e$  is used. Another point regarding the matrices is that they are not symmetric. They are solved iteratively with the general minimal residual method (GMRES) [31] instead of the conjugate gradient method, and our block-based preconditioning strategy relies on the SuperLU libraries of direct solvers for sparse matrices [32]. Finally, the finite element/finite Fourier series spatial representation is largely the same as in Ref. [17]; though, the nodes of the Lagrange polynomials now coincide with the Gauss-Lobatto-Legendre quadrature nodes, so that the elements are spectral [33].

### 3. ANALYSIS

Our numerical analysis considers the linear response for plane waves in an infinite uniform background. In some cases, we include the effects of uniform background electron flow that differs from background ion flow ( $V_{e0} \neq V_0$ ) in the advance of magnetic field. This provides an important check on electron flow, but it is ad hoc in that the associated current density is not consistent with Eq. (5) and uniform background magnetic field. We also simplify temperature evolution such that both the background and perturbed electron pressures are fixed fractions ( $f_e$ ) of the total background and perturbed pressures, respectively. For the normal modes of our system, scaling  $f_e$  from 0 to 1 only changes the influence of the ion gyroviscous term.

In the following subsection, we find eigenvalues of the implicit leapfrog advance explicitly for limited systems and numerically for the full system. The second subsection considers differential approximation for specific modes to provide greater insight on the stability properties of the system.

### 3.1 Plane-Wave Modes of the Algorithm

Our plane-wave analysis considers all perturbed fields to vary as  $e^{iky}$  with the background magnetic field in the  $y$ - $z$  plane. Further simplification results from assuming adiabatic responses with the same ratio of specific heats ( $\Gamma$ ) for both species. This allows us to combine the perturbed number density and temperature equations into a perturbed pressure equation. The algebraic state vector then has three complex coefficients for velocity, two for magnetic field after applying the divergence constraint, and one for pressure. We normalize  $\mathbf{B}$  with respect to the background magnitude  $B_0$ ,  $\mathbf{V}$  with respect to the Alfvén speed  $v_A = B_0(\mu_0 mn)^{-1/2}$ , time with respect to  $\Omega_i^{-1}$ , and length with respect to the ion skin depth  $d_i = c\omega_i^{-1}$ , where the ion plasma frequency for singly charged ions is defined by  $\omega_i^2 = ne^2/\epsilon_0 m_i$ . With  $\beta \equiv \mu_0 P_0 / B_0^2$ , the linear system is then

$$\left(\frac{1}{\Delta t} + ikV_0\theta_v - \Delta t\underline{\underline{L}}\right)(\underline{v}^{j+1} - \underline{v}^j) = -ikV_0\underline{v}^j + ik\begin{pmatrix} c & 0 & 0 \\ 0 & -s & -\beta \\ 0 & c & 0 \end{pmatrix}\begin{pmatrix} b_x \\ b_z \\ p \end{pmatrix}^{j+1/2} + \frac{1}{2}\underline{\underline{F}}(\underline{v}^{j+1} + \underline{v}^j) \quad (14)$$

$$\left[\frac{1}{\Delta t} + ikV_{e0}\theta_b + \left(\frac{m_e}{m_i\Delta t} + D_\eta\theta_\eta\right)k^2\right]\left(\underline{b}^{j+3/2} - \underline{b}^{j+1/2}\right) = -ikV_{e0}\underline{b}^{j+1/2} + ik\begin{pmatrix} c & 0 & 0 \\ 0 & -s & c \end{pmatrix}\underline{v}^{j+1} - D_\eta k^2 \underline{b}^{j+1/2} + \frac{k^2 c}{2}\begin{pmatrix} 0 & 1 \\ -1 & 0 \end{pmatrix}\left(\underline{b}^{j+3/2} + \underline{b}^{j+1/2}\right) \quad (15)$$

$$\left(\frac{1}{\Delta t} + ikV_0\theta_p\right)\left(p^{j+3/2} - p^{j+1/2}\right) = -ikV_0 p^{j+1/2} - ik\Gamma v_y^{j+1}, \quad (16)$$

where  $\underline{v} = (v_x, v_y, v_z)^T$  and  $\underline{b} = (b_x, b_z)^T$ ;  $\theta_v$ ,  $\theta_b$ ,  $\theta_p$ , and  $\theta_\eta$  are temporal centering coefficients for advection and resistive diffusion; and  $D_\eta \equiv \eta/\mu_0 d_i^2 \Omega_i$ . The orientation of the background magnetic field appears through the cosine ( $c$ ) and sine ( $s$ ) of the angle it makes with respect to  $\hat{\mathbf{y}}$ . The matrices that represent the semi-implicit operator and gyroviscous force are, respectively,

$$\underline{\underline{L}} = -C_0 k^2 \begin{pmatrix} c^2 & 0 & 0 \\ 0 & s^2 + \Gamma\beta & -cs \\ 0 & -cs & c^2 \end{pmatrix} \quad (17)$$

$$\underline{\underline{F}} = \frac{(1-f_e)\beta k^2}{4} \begin{pmatrix} 0 & -2s(1+3c^2) & c[1+3(c^2-s^2)] \\ 2s(1+3c^2) & 0 & 0 \\ -c[1+3(c^2-s^2)] & 0 & 0 \end{pmatrix}. \quad (18)$$

Properties of the advance are determined from the eigenvalues ( $\lambda$ ) of the time-step operation that is defined by combining Eqs. (14-18). With the staggering, the modes satisfy

$$\begin{pmatrix} \underline{v}^{j+1} \\ \underline{b}^{j+3/2} \\ \underline{p}^{j+3/2} \end{pmatrix} = \lambda \begin{pmatrix} \underline{v}^j \\ \underline{b}^{j+1/2} \\ \underline{p}^{j+1/2} \end{pmatrix}, \quad (19)$$

and there as many as six nontrivial modes for each set of physical and numerical parameters.

Before evaluating the full dispersion relation numerically, we consider the properties of the system in different limits. For sufficiently large wavenumber and small  $\beta$ , the ions do not respond, and nontrivial electron-MHD modes result from the coupling of  $b_x$  and  $b_z$ . The two eigenvalues of the dispersion relation from Eq. (15) are

$$\lambda = \frac{1 + \frac{m_e}{m_i} k^2 - ik\Delta t(1-\theta_b)V_{e0} \pm i \frac{k^2 c \Delta t}{2} - D_\eta k^2 \Delta t(1-\theta_\eta)}{1 + \frac{m_e}{m_i} k^2 + ik\Delta t \theta_b V_{e0} \mp i \frac{k^2 c \Delta t}{2} + D_\eta k^2 \Delta t}. \quad (20)$$

In the absence of resistive diffusion, and with centered advection ( $\theta_b = 1/2$ ), the numerator and denominator are complex conjugates. Numerical stability in the sense of  $|\lambda| \leq 1$  is expected and achieved for all values of  $\Delta t$  in this case, because it limits to a Crank-Nicolson advance. The algorithm is also numerically stable with resistive dissipation, provided that  $\theta_\eta \geq 1/2$ .

The MHD limit of Eqs. (14-16) is obtained at small wavenumber (normalized- $k \ll 1$ ) with cold ions ( $f_e \rightarrow 1$ ) and no background current density. Here, the gyroviscous term in (14) and the Hall and electron inertia terms in (15) are negligible. The primary difference between this limit of our system and other semi-implicit algorithms for MHD [15, 17, 34] is the use of implicit advection instead of explicit predictor-corrector or upwinding. For convenience, we use the same centering coefficient for advection in all equations,  $\theta_v = \theta_b = \theta_p = \theta$ . Substituting (15) and (16) into (14) provides a homogenous algebraic system for  $\underline{v}$ , where the first row and column are identically zero, except for the diagonal element. Setting this diagonal element to zero provides the dispersion relation for the shear Alfvén mode. The determinant of the remaining symmetric 2x2 submatrix provides the dispersion relations for the fast- and sound-wave branches. Their factoring is not readily apparent when  $D_\eta \neq 0$ , but the numerical dispersion relation has a form that mimics the analytical system with nonzero resistivity. When  $D_\eta = 0$ , the dispersion relation for each of the three factored modes has the form

$$\frac{[(\lambda-1)(1+i\xi\theta)+i\xi]^2}{C_0(\lambda-1)[(\lambda-1)(1+i\xi\theta)+i\xi]+\lambda} + \chi^2 = 0, \quad (21)$$

where  $\xi \equiv k\Delta t V_0$ ,  $\chi \equiv k\Delta t v_\phi$ , and the normalized shear-, fast-, and sound-wave phase velocities are given by

$$v_\phi^2 = \begin{cases} c^2 \\ \frac{1}{2} \left[ 1 + \Gamma\beta \pm \sqrt{1 + 2(s^2 - c^2)\Gamma\beta + \Gamma^2\beta^2} \right] \end{cases}. \quad (22)$$

Equation (21) is quadratic in  $\lambda-1$ , and the discriminant simplifies to a real number for centered advection,  $\theta = 1/2$ :

$$\lambda-1 = \frac{-\left[(1+i\xi C_0)\chi^2 + 2i\xi - \xi^2\right] \pm \chi \sqrt{(1-4C_0 - \xi^2 C_0^2)\chi^2 - 4 - \xi^2}}{2(1+i\xi/2) \left[ C_0\chi^2 + (1+i\xi/2) \right]}. \quad (23)$$

As in semi-implicit computation without flow, setting the coefficient  $C_0 \geq 1/4$  leads to  $|\lambda|=1$  independent of  $\Delta t$ . With  $C_0 = 1/4$ , the leading terms of (23) for a small- $\Delta t$  expansion produce

$$\lambda = 1 - i\xi \pm i\chi - \xi^2/2 - \chi^2/2 \pm \xi\chi + O(\Delta t^3), \quad (24)$$

which is the expansion of  $e^{-i\omega\Delta t}$  to second order for  $\omega\Delta t = \xi \mp \chi$ . Evaluation with  $\theta \neq 1/2$  leads to instability, as shown below with numerical evaluation.

A third limit is for parallel propagation ( $c \rightarrow 1$ ,  $s \rightarrow 0$ ) without flow or dissipation but considering all wavelengths and  $\beta$ -values. Electron inertia does not change the stability result and is dropped for clarity. The sound wave factors readily in this case. Using  $\chi = k\Delta t$  (the CFL number for Alfvén waves with our normalization), defining  $\beta_i \equiv (1 - f_e)\beta$ , and setting the remaining factor of the dispersion relation to zero produces

$$(\lambda-1)^2(1+C_0\chi^2) \pm i(\lambda^2-1)\left(\frac{k\chi}{2}\right)\left[1+C_0\chi^2+\beta_i\right] - (\lambda+1)^2\left(\frac{k^2\chi^2\beta_i}{4}\right) + \lambda\chi^2 = 0. \quad (25)$$

This relation leads to four circularly polarized waves [6] that are influenced by the Hall term in Ohm's law and gyroviscosity in the flow-velocity equation. The coefficient of  $\lambda^2$  is the complex conjugate of the coefficient of  $\lambda^0$ , and the  $\lambda^1$ -coefficient is real. Applying the same condition of  $C_0 \geq 1/4$  makes the advance stable and free of numerical dissipation for all  $\Delta t$ -values across the transition from MHD to electron-MHD. With  $C_0 = 1/4$ , the eigenvalues are

$$\lambda = \frac{1 - \frac{\chi^2}{4}(1 - \beta_i k^2) \pm i\chi \sqrt{1 + \frac{k^2}{4}\left(1 - \beta_i + \frac{\chi^2}{4}\right)^2 + \frac{k^2\chi^2\beta_i}{4}}}{1 + \frac{\chi^2}{4}(1 - \beta_i k^2) \pm \frac{i}{2}k\chi\left(1 + \beta_i + \frac{\chi^2}{4}\right)}, \quad (26)$$

where all four sign combinations are solutions. Expanding (26) in powers of  $\chi$  agrees with  $e^{-i\omega\Delta t}$  for the analytical eigenvalues,  $\omega = \pm k\sqrt{1 + k^2(1 - \beta_i)^2/4} \pm k^2(1 + \beta_i)/2$ , through second order in  $\Delta t$ .

Having considered limits of the implicit leapfrog, we turn to numerical evaluation of the eigenmodes for more general cases. Here, we evaluate coefficients of matrices from Eqs. (14-16) for various sets of parameters. The corresponding time-step matrix in each case is constructed by applying the matrix that represents the explicit computations for one step to the result of a previous step (or to the identity matrix for the first step) then applying the inverse of the matrix representing the respective implicit computations. With the implicit leapfrog, there are three such steps, one to advance  $\underline{v}$ , one to advance  $\underline{b}$ , and one to advance  $p$ . With Crank-Nicolson, there is only one step to advance all fields. The complex eigenvalues of the time-step matrix are then determined with LAPACK routines [35]. The argument of an eigenvalue and the logarithm of its magnitude provide predictions for frequency and growth rate, respectively.

We first confirm the influence of the coefficient of the semi-implicit operator and the centering parameters in more general conditions than the limiting cases. The background magnetic field is placed at a  $45^\circ$  angle with respect to  $\mathbf{k}$ ,  $\beta = 0.15$ ,  $\Gamma = 5/3$ ,  $f_e = 1/2$ ,  $m_e = 0$ , and background ion and electron flows are 20% and 30% of the Alfvén speed, respectively. In Fig. 1a, we show numerical results for the predicted  $\text{Re}(\omega)$  with  $\Delta t = 1$ , centered advection  $\theta_v = \theta_b = \theta_p = \theta = 1/2$ ,  $C_0 = 1/4$ , and no resistive dissipation. Waves propagating in the positive and negative  $y$ -directions are not symmetric about  $\text{Re}(\omega) = 0$  due to the flows. Numerical dispersion that is characteristic of implicit methods for waves is evident in the fast modes at large- $k$ . Results for  $\text{Im}(\omega)$  for these parameters (Fig. 1b) show only roundoff error from the computations. Increasing both  $\Delta t$  and the maximum  $k$ -value to 1000, for example, also produces only roundoff error for  $\text{Im}(\omega)$ , confirming numerical stability for arbitrarily large  $\Delta t$ -values. Figures 1c and 1d show results for  $\text{Im}(\omega)$  and  $\Delta t = 1$  when  $C_0 < 1/4$  and  $\theta > 1/2$ , respectively. The nontrivial  $\text{Im}(\omega)$ -values that are greater than zero indicate numerical instability. Advection with  $\theta < 1/2$  also shows numerical instability.<sup>1</sup> Results in Fig. 2 show the effects of resistive dissipation with  $D_\eta = 0.2$  and parameters that are stable for the ideal system. There is only damping with centered resistive dissipation,  $\theta_\eta = 1/2$  (Fig. 2a and confirmed with large  $\Delta t$  and  $k$ -values), but numerical instability is encountered for  $k > 2.6$  with  $\theta_\eta = 1/4$  (Fig. 2b).

Eigenmode analysis for numerically stable parameters with  $V_{e0} = V_0$  also provides useful verification exercises for the NIMROD implementation. With sufficient spatial resolution, NIMROD and Eqs. (14-16) are expected to produce the same behavior at any  $\Delta t$ -value. We consider nearly parallel propagation with  $\hat{\mathbf{k}} \cdot \hat{\mathbf{b}} = 0.992$  and  $\beta = 0.15$  and nearly perpendicular propagation with  $\hat{\mathbf{k}} \cdot \hat{\mathbf{b}} = 0.125$  and  $\beta = 0.6$ . The time-step values of  $\Delta t = 0.5$  for the first set and  $\Delta t = 1.5$  for the second are chosen such that  $\omega\Delta t \leq 2$  for the fastest waves. Spatial truncation error is made negligible in the NIMROD computations by using four finite elements with basis functions of polynomial degree six along the direction of propagation. Each computation is

<sup>1</sup> Analysis for the two-fluid model with predictor-corrector advection that is successful for semi-implicit MHD [34] shows numerical instability for wavelengths approaching the ion skin depth, essentially independent of  $\Delta t$ .

initialized from one eigenvector found from the LAPACK analysis, and the eigenvectors reflect the temporal shift between flow velocity and the other components at finite  $\Delta t$ -values. The NIMROD results are checked for maintaining a single sine wave in each physical component, and the frequency is measured from ten wave periods. The agreement shown in Fig. 3 confirms the implicit leapfrog implementation for these conditions. The results have been computed with  $V_{e0} = V_0 = 0.2$ , so the positive and negative-going waves are again not symmetric about  $\text{Re}(\omega) = 0$ . In fact, the negative-going slow wave and kinetic Alfvén wave (KAW) in Fig. 3b are carried in the positive direction by the large flow for at least some of the  $k$ -values. For nearly parallel propagation, there is significant numerical dispersion in the fast whistler wave (Fig. 3a), which behaves analytically as  $\omega \sim k^2$  for  $k > 1$ . There is also significant numerical dispersion in the fast compressive wave in Fig. 3b, which is not dispersive analytically for this range of wavenumber. However, what is important here is that the implementation agrees with the analysis.

We also compute numerical eigenvalues to compare the accuracy of the implicit leapfrog algorithm with that of the time-centered Crank-Nicolson algorithm for the full system. The temporal staggering makes the implicit leapfrog consistent of order  $\Delta t^2$ , but Ref. [36] emphasizes that any form of splitting for problems with multiple time-scales may lead to loss of accuracy when  $\Delta t$  is larger than the time-scale of each process. Results with  $\Delta t = 0.5$ , presented in Fig. 4a, show that there is significant numerical dispersion in the fast whistler mode for both algorithms where  $\omega\Delta t > 1$ . The accuracy of the intermediate-frequency wave is comparable for the two algorithms through the transition at  $k \approx 1.2$ , where the ions lose magnetization in the two-fluid model. For the lowest-frequency mode, we expect a transition to the slow circularly polarized mode that is influenced by gyroviscosity. The implicit leapfrog forces  $\text{Re}(\omega)$  for this mode toward zero at large- $k$ , particularly for the larger- $\Delta t$  case shown in Fig. 4b, while the Crank-Nicolson algorithm is more accurate. For this mode, effects from the ion cyclotron resonance appearing through the two-fluid Ohm's law are important for the transition. However, the relevant ion motion with the implicit leapfrog algorithm is suppressed for  $k\Delta t \geq 1$  by the semi-implicit operator, which is based on MHD. Results for nearly perpendicular propagation at  $\Delta t = 1.5$  and  $\Delta t = 4$  in Fig. 5 show comparable accuracy for the two algorithms for all modes throughout the wavenumber range.

### 3.2 Differential Approximation

The von Neumann analysis described in the previous section shows that the algorithm can be numerically unstable when advection is not centered and with forward differencing of resistive diffusion. With centered advection, Hall, and gyroviscous terms, the results indicate the criterion  $C_0 \geq 1/4$  for stability at arbitrarily large  $\Delta t$ -values, which is the same criterion for the semi-implicit method applied to a basic hyperbolic wave equation [26]. To provide insight regarding these results and increase confidence that our set of numerical evaluations are representative, we turn to differential approximation. We consider the same normalized linear system described for Section 3.1 and apply differential approximation in limits that illustrate the stability properties. We follow the prescription of Ref. [26] keeping terms that require no additional initial conditions relative to the original PDE problem. A possibly unique aspect, however, is to address the temporal staggering through synchronization terms in the differential approximation. We find this approach to be more tractable and productive than expanding the entire system about a single time, which is illustrated in Appendix B for a basic hyperbolic system.

To appreciate the effects of the centering coefficients, we consider propagation perpendicular to the magnetic field in the limit of low wavenumber,  $V_{e0} = V_0$ , and  $\beta \rightarrow 0$ . The algorithm for the normalized linear system reduces to

$$\left(1 - \Delta t^2 C_0 \frac{\partial^2}{\partial y^2}\right) \left(\frac{v^{j+1} - v^j}{\Delta t}\right) = -V_0 \frac{\partial}{\partial y} \left[\theta_v v^{j+1} + (1 - \theta_v) v^j\right] - \frac{\partial}{\partial y} b^{j+1/2} \quad (27)$$

$$\begin{aligned} \frac{b^{j+3/2} - b^{j+1/2}}{\Delta t} = & -V_0 \frac{\partial}{\partial y} \left[\theta_b b^{j+3/2} + (1 - \theta_b) b^{j+1/2}\right] \\ & + D_\eta \frac{\partial^2}{\partial y^2} \left[\theta_\eta b^{j+3/2} + (1 - \theta_\eta) b^{j+1/2}\right] - \frac{\partial}{\partial y} v^{j+1} \quad , \end{aligned} \quad (28)$$

where  $v$  refers to just the  $y$ -component of flow velocity, and  $b$  is just the  $z$ -component. We expand  $v$  in time about  $t_{1/2} = (j + 1/2)\Delta t$  and  $b$  about  $t_1 = (j + 1)\Delta t$ . Thus, while there are no truncation errors from the last terms on the right sides of Eqs. (27-28), they are expanded to account for synchronization of the two differential equations. Keeping the terms that require no additional initial conditions, we have

$$\left(1 - \Delta t^2 C_0 \frac{\partial^2}{\partial y^2}\right) \frac{\partial v}{\partial t} \Big|_{t_{1/2}} = -V_0 \frac{\partial}{\partial y} \left[v + \Delta t \left(\theta_v - \frac{1}{2}\right) \frac{\partial v}{\partial t}\right]_{t_{1/2}} - \frac{\partial}{\partial y} \left(b - \frac{\Delta t}{2} \frac{\partial b}{\partial t}\right)_{t_1} \quad (29)$$

$$\frac{\partial b}{\partial t} \Big|_{t_1} = -V_0 \frac{\partial}{\partial y} \left[b + \Delta t \left(\theta_b - \frac{1}{2}\right) \frac{\partial b}{\partial t}\right]_{t_1} + D_\eta \frac{\partial^2}{\partial y^2} \left[b + \Delta t \left(\theta_\eta - \frac{1}{2}\right) \frac{\partial b}{\partial t}\right]_{t_1} - \frac{\partial}{\partial y} \left(v + \frac{\Delta t}{2} \frac{\partial v}{\partial t}\right)_{t_{1/2}} \quad , \quad (30)$$

showing explicitly—and only once—the times at which fields and derivatives are evaluated. Apart from the term for the semi-implicit operator, the system (29-30) is the  $\Gamma$ -form of the first differential approximation [25] when not all of the numerical  $\theta$ -coefficients are set to  $1/2$ .

We first consider the effects of varying  $\theta_\eta$  simply by moving the resistive truncation term to the left side of Eq. (30). For a bounded system with homogeneous Dirichlet or Neumann boundary conditions, the operator acting on the  $\partial b / \partial t$  is positive when  $\theta_\eta \geq 1/2$  in the sense that

$$\int b \left[1 - \Delta t D_\eta \left(\theta_\eta - \frac{1}{2}\right) \frac{\partial^2}{\partial y^2}\right] \frac{\partial b}{\partial t} dy = \frac{1}{2} \frac{d}{dt} \int \left[b^2 + \Delta t D_\eta \left(\theta_\eta - \frac{1}{2}\right) \left(\frac{\partial b}{\partial y}\right)^2\right] dy \quad , \quad (31)$$

and the integral on the right is positive for nontrivial fields. Thus, the effect of backward differencing is to numerically increase inductance. In contrast, the integral may be non-positive with forward differencing for sufficiently large  $\Delta t$ -values, in which case the differential approximation is an ill-posed equation, hence the method is numerically unstable. We will not include resistivity throughout, but the semi-implicit operator has a similar role in keeping the effective operator for inertia positive [15, 26].

The significance of centering advection is found by considering Eqs. (29-30) through order  $\Delta t$ , i.e. the first differential approximation when  $\theta_v, \theta_b \neq 1/2$ . Here, we set  $\theta_\eta = 1/2$  for tractability. Substituting  $v = (Z_+ + Z_-)/2$  and  $b = (Z_+ - Z_-)/2$  with new variables for the sum

( $Z_+$ ) and difference ( $Z_-$ ) of  $v$  and  $b$  leads to two differential equations that can be written compactly as

$$\begin{aligned} \frac{\partial Z_{\pm}}{\partial t} = & -V_0 \frac{\partial}{\partial y} Z_{\pm} \mp \frac{\partial}{\partial y} Z_{\pm} \pm \frac{D_{\eta}}{2} \frac{\partial^2}{\partial y^2} (Z_+ - Z_-) \\ & + \frac{\Delta t}{2} (V_0^2 \pm V_0) (\theta_v + \theta_b - 1) \frac{\partial^2}{\partial y^2} Z_{\pm} - \frac{\Delta t}{2} \left[ V_0^2 (\theta_b - \theta_v) \mp V_0 (\theta_b - \theta_v + 1) + 1 \right] \frac{\partial^2}{\partial y^2} Z_{\mp} \quad (32) \\ & + \frac{D_{\eta} \Delta t}{2} \left[ \frac{1}{2} \mp V_0 \left( \theta_b - \frac{1}{2} \right) \right] \frac{\partial^3}{\partial y^3} (Z_+ - Z_-) . \end{aligned}$$

The terms of order  $\Delta t^0$  represent two waves that propagate in opposite directions relative to the background flow with coupling through resistive dissipation. The first term of order  $\Delta t$  is diffusive when its coefficient is positive but leads to an ill-posed problem when its coefficient is negative. For flow speeds that are smaller than the wave speed, which is unity after our normalization, the sign of the coefficient is different for the two different waves, and one response is numerically unstable if  $\theta_v + \theta_b \neq 1$ . This agrees with our finding from von Neumann analysis that either forward or backward differencing in all equations is unstable. With flow speeds larger than the wave speed, Eq. (32) predicts damping for backward differencing, and this has been confirmed with numerical evaluation of eigenvalues for  $V_0 > 1$ . The second term of order  $\Delta t$  includes truncation errors that can be eliminated with  $\theta_v = \theta_b$ . Together, the findings lead to the conclusion that centered advection for all advances is needed. The remaining terms of order  $\Delta t$  in Eq. (32) result from synchronization and are not indicative of first-order accuracy.

We also use Eqs. (29-30) to examine the compatibility of centered advection and the semi-implicit operator. Here, we set  $D_{\eta} = 0$  and keep the term of order  $\Delta t^2$ . Differentiating Eq. (29) in time and Eq. (30) in space to eliminate the first temporal derivative of  $b$  leads to the intermediate step

$$\left( 1 - \Delta t^2 C_0 \frac{\partial^2}{\partial y^2} \right) \frac{\partial^2 v}{\partial t^2} = -V_0 \frac{\partial}{\partial y} \frac{\partial v}{\partial t} + \frac{\partial^2}{\partial y^2} \left( v + \frac{\Delta t}{2} \frac{\partial v}{\partial t} \right) + \frac{\Delta t}{2} \frac{\partial}{\partial y} \frac{\partial^2 b}{\partial t^2} + V_0 \frac{\partial}{\partial y} \left( \frac{\partial}{\partial y} b \right) .$$

Using (29) to replace the spatial derivative of  $b$  in the last term and a temporal derivative of Eq. (30) to eliminate  $b$  leads to

$$\left[ 1 - \Delta t^2 \left( C_0 - \frac{1}{4} \right) \frac{\partial^2}{\partial y^2} \right] \frac{\partial^2 v}{\partial t^2} + V_0 \left( 2 - \Delta t^2 C_0 \frac{\partial^2}{\partial y^2} \right) \frac{\partial}{\partial y} \frac{\partial v}{\partial t} + (V_0^2 - 1) \frac{\partial^2}{\partial y^2} v = 0 . \quad (33)$$

Similar to the centering coefficient for the implicit resistive diffusion, this wave equation has a positive operator acting on its highest temporal derivative for all  $\Delta t$ -values when  $C_0 \geq 1/4$ .

Considering infinite or periodic systems, where Fourier expansion is appropriate, solutions of the characteristic equation for each wavenumber,

$$\omega_k = \frac{kV_0 \left(1 + \frac{C_0}{2} k^2 \Delta t^2\right) \pm k \sqrt{1 + k^2 \Delta t^2 \left(C_0 + \frac{V_0^2}{4} - \frac{1}{4}\right) + \frac{C_0^2}{4} V_0^2 k^4 \Delta t^4}}{1 + \left(C_0 - \frac{1}{4}\right) k^2 \Delta t^2} , \quad (34)$$

are real for all  $\Delta t$ -values when  $C_0 \geq 1/4$ . Centered advection therefore maintains the dissipation-free property of the semi-implicit advance, which is also evident from Eq. (23) and the results shown in Fig. 1b.

With this approach, we are also able to see how physically dispersive contributions are compatible with the semi-implicit operator when they are centered in the advances of the respective fields. We consider parallel propagation in the limit  $V_{e0} = V_0 = 0$  and  $\beta \rightarrow 0$  without restricting to low wavenumber. Here the difference equations simplify to

$$\left(\frac{1}{\Delta t} - \Delta t C_0 \frac{\partial^2}{\partial y^2}\right) (\underline{v}^{j+1} - \underline{v}^j) = \frac{\partial}{\partial y} \underline{b}^{j+1/2} \quad (35)$$

$$\frac{1}{\Delta t} \left(1 - \frac{m_e}{m_i} \frac{\partial^2}{\partial y^2}\right) (\underline{b}^{j+3/2} - \underline{b}^{j+1/2}) = \frac{\partial}{\partial y} \underline{v}^{j+1} + \frac{1}{2} \begin{pmatrix} 0 & -1 \\ 1 & 0 \end{pmatrix} \frac{\partial^2}{\partial y^2} (\underline{b}^{j+3/2} + \underline{b}^{j+1/2}) , \quad (36)$$

where the vectors  $\underline{v}$  and  $\underline{b}$  have  $x$ - and  $z$ -components. The differential approximation requiring the same initial conditions as the original differential equation is

$$\left(1 - \Delta t^2 C_0 \frac{\partial^2}{\partial y^2}\right) \frac{\partial}{\partial t} \underline{v} = \frac{\partial}{\partial y} \left(\underline{b} - \frac{\Delta t}{2} \frac{\partial}{\partial t} \underline{b}\right) \quad (37)$$

$$\left(1 - \frac{m_e}{m_i} \frac{\partial^2}{\partial y^2}\right) \frac{\partial}{\partial t} \underline{b} = \frac{\partial}{\partial y} \left(\underline{v} + \frac{\Delta t}{2} \frac{\partial}{\partial t} \underline{v}\right) + \begin{pmatrix} 0 & -1 \\ 1 & 0 \end{pmatrix} \frac{\partial^2}{\partial y^2} \underline{b} . \quad (38)$$

With manipulations that are similar to the previous example of MHD with flow, we find the wave equation

$$\left[ \left(1 - \Delta t^2 C_0 \frac{\partial^2}{\partial y^2}\right) \left(1 - \frac{m_e}{m_i} \frac{\partial^2}{\partial y^2}\right) + \frac{\Delta t^2}{4} \frac{\partial^2}{\partial y^2} \right] \frac{\partial^2}{\partial t^2} \underline{b} = - \left(1 - \Delta t^2 C_0 \frac{\partial^2}{\partial y^2}\right) \begin{pmatrix} 0 & 1 \\ -1 & 0 \end{pmatrix} \frac{\partial^2}{\partial y^2} \frac{\partial}{\partial t} \underline{b} + \frac{\partial^2}{\partial y^2} \underline{b} . \quad (39)$$

More boundary conditions would be needed for this equation than for the original PDE, but with homogeneous Dirichlet and Neumann conditions, the spatial operator acting on this highest temporal derivative is again positive for  $C_0 \geq 1/4$ . Electron mass contributes to this property but is not required. With Fourier expansion in space, the solutions of the characteristic equation for  $\omega_k^2$  are real and positive for  $C_0 \geq 1/4$ . Propagation without damping or instability is again consistent with the findings of Sect. 3.1.

#### 4. LINEAR BENCHMARK AND EXAMPLE NONLINEAR APPLICATION

The analysis of Sect. 3 confirms critical numerical stability properties of the implicit leapfrog algorithm and provides information on accuracy. However, plane-wave propagation in uniform plasma is not representative of applications of interest. Here, we consider a two-dimensional linear tearing instability in slab geometry and present a nonlinear three-dimensional application to the internal kink mode in toroidal geometry. Parameters in this section are in MKS units.

##### 4.1 Linear Tearing Instability

When computed with experimentally relevant conditions, tearing instabilities exercise an algorithm's ability to reproduce balances over multiple temporal and spatial scales. Like other MHD instabilities, they are driven by gradients in the parallel current density profile or in the pressure profile. The eigenfunctions extend over macroscopic scales but are sensitive to a resonance condition at the surface where  $\mathbf{k} \cdot \mathbf{B}_0 = 0$ ,  $\mathbf{k}$  being the wavenumber vector with respect to the periodic coordinates. In the vicinity of the resonance, rapid variations in the direction normal to the surface allow the mode to reconnect magnetic field-lines, even in high temperature plasma where resistivity is small. Away from this surface, bending of magnetic field provides a restoring force that is analogous to the shear Alfvén wave response. The slow evolution regulated by reconnection allows forces to balance on the macroscopic scale; hence, the multi-scale nature of the instability. The two-fluid model allows electron flows to separate on an intermediate scale through forces that govern the dispersive whistler and KAW waves [37], allowing faster reconnection. Recent analytical theory [3, 38] clarifies transitions across the different parameter regimes. The derivation in Ref. [3] uses a separation between the reconnection and ion scales and between the ion and macroscopic scales. It is valid across the entire ranges of  $\beta$  and the instability parameter  $\Delta'$ , but the use of two asymptotic matchings precludes the MHD limit, where the reconnection scale extends to the ion scale. Reference [38] uses only one matching by assuming a minimal  $\beta$  and allows for the transition to MHD with decreasing  $d_i$ . Both derivations are useful for our benchmarking.

The two theories use equilibria where the in-plane component of  $\mathbf{B}_0$  varies as a hyperbolic tangent,  $B_y(x) = B_{y_\infty} \tanh(x/L)$ , and the domain in the inhomogeneous direction is not bounded. The pressure is uniform, so equilibrium diamagnetic drift effects are not considered. With this class of equilibria, the instability parameter has the simple form  $\Delta'L = 2/kL - 2kL$ . This is convenient analytically, but NIMROD computations must approximate the domain with walls at finite locations  $|x| > L$ . Through experimentation, we find that  $-6L \leq x \leq 6L$  is sufficient, but this implies a fourth spatial scale in the computational domain. For comparison with Ref. [3], our largest- $\beta$  computation has the reconnection scale  $\Delta'\delta^2$  [39] nearly 1000 times smaller than  $L$ , where  $\delta$  is the generalized skin depth  $\sqrt{d_e^2 + \eta/\mu_0\gamma}$  with  $\gamma$  being the growth rate. To obtain spatial convergence, we use meshes of up to 240 biquartic elements in the  $x$ -direction with packing near the resonant surface such that the smallest elements have width comparable to  $\Delta'\delta^2$ .

Converged growth rates from NIMROD computations are compared with the two theories in Fig. 6. The equilibria have a large guide field ( $B_z$ ) that is 25 or 50 times larger than  $B_{y_\infty}$ ;

though, this is not required for the more recent theory. For the first set,  $kd_i$  is fixed at 2.3, and pressure is varied to scan the ‘sound gyroradius,’  $\rho_s = d_i \sqrt{\Gamma\beta}$ , which governs the transition from the shear Alfvén wave to the KAW response. The comparison with solutions of Eq. (73) of Ref. [3] is shown in Fig. 6a for computations with and without finite electron inertia. At small values of  $k\rho_s$ , the computations show the transition between resistive MHD and two-fluid reconnection. At large  $k\rho_s$ , the combined effects of compression and diffusion of the out-of-plane component of perturbed magnetic field limits the growth rate—see Ref. [3]. Quantitative comparison at intermediate to large  $k\rho_s$  is influenced by the marginal scale separation of  $\delta/L \cong 8\%$  that results with  $S = \mu_0 v_A / \eta k = 1.79 \times 10^7$ . The less restrictive assumption of  $S^{-2/5} \ll \beta$  required for the derivation of Ref. [38] is well satisfied in the computations presented in Fig. 6b, where  $S = 3.50 \times 10^7$  and  $\beta = 0.05$  (with the definition from Sect. 3). The transition from MHD is described by Eqs. (85-87) of Ref. [38], and the quantitative agreement of the computations is within 2.3%. All computations in this second set include electron inertia, but  $d_e$  is at least an order of magnitude smaller than  $\delta$  and does not affect the growth rate.

A representative eigenfunction from the  $kd_i = 0.238$  computation of Fig. 6b is shown in Fig. 7 to display the range of spatial scales. The component of perturbed  $\mathbf{B}$  in the direction of inhomogeneity shows the influence of the equilibrium and boundary scales, in addition to evidence of reconnection by its nonzero value at the resonant surface,  $x = 0$ . Ion and electron flows that are perpendicular to the guide field show characteristic two-fluid separation below the  $x = \rho_s$  scale;  $\rho_s = 0.09L$  in this case. Within the reconnection scale of  $\Delta'\delta^2 = 0.007L$ , current density parallel to the guide field is associated with the localized resistive magnetic diffusion for reconnection.

The temporal convergence properties of this calculation show second-order accuracy for centered dissipation,  $\theta_\eta = 1/2$ , and sufficiently small time-step. The error relative to a reference computation is shown in Fig. 8. As  $\Delta t$  is increased from the converged limit, the computed growth rate is initially below the converged value. At large  $\Delta t$ -values, the error is positive, hence the break in the trace. For accuracy of order 1%, the implicit leapfrog needs  $\Delta t \cong 0.03\gamma^{-1}$  for this two-fluid computation, which is similar to the performance of our semi-implicit algorithm on a resistive MHD tearing mode in cylindrical geometry [17]. At the largest  $\Delta t$ -values, distortion of the eigenfunctions is most evident in the perpendicular ion flows near the ion-separation scales. When scaling by the peak value for the electron velocity, the perpendicular ion velocity in the largest- $\Delta t$  computation is approximately 2.6 times smaller than what is shown in Fig. 7b. This is likely due to the effect of the semi-implicit operator in the flow velocity advance. The scaled trace of the perpendicular electron velocity is indistinguishable from the small time-step result, however, so the magnetic field is unaffected. Lastly, although the spatial resolution in our computations is finer, we note that minimal resolution of the tearing region is some fraction of  $\Delta'\delta^2$ . Fast compressional waves of the system would traverse these smallest computational scales more than  $10^6$  times during a period of  $\Delta t \cong 0.03\gamma^{-1}$ .

#### 4.2 Nonlinear Internal Kink

As an example three-dimensional application of the algorithm, we consider the nonlinear evolution of the internal kink mode in a tokamak. An important result from reduced two-fluid

modeling with helical symmetry in cylindrical geometry is that the exponentiation rate of kinetic energy increases during the nonlinear phase while the geometry of the reconnection changes from a current sheet to an ‘X-point’ [40]. This result has recently been confirmed in helically symmetric computations with a non-reduced model [41], which can reproduce all shearing and compressive responses. Here, we show a similar computation in toroidal geometry, which breaks the helical symmetry. The configuration has a circular cross-section with moderate aspect ratio  $R/a = 4$ , where  $R$  and  $a$  are the major and minor radii of the torus, respectively. Like Ref. [40], the MHD equilibrium has uniform pressure to avoid equilibrium diamagnetic effects, and  $\beta = 2.5 \times 10^{-3}$  from electron thermal energy only. The current profile is described by  $RB_\phi = 3.44 + 0.12(1 - \Psi) + 0.064\Psi(\Psi - 1)$ , where  $\Psi$  is the normalized poloidal flux function that is zero at the magnetic axis and unity at the wall. This makes  $q(0) = 0.97$  and  $q(1) = 1.61$ , where  $q(\Psi)$  is the magnetic winding profile. Physical parameters are chosen such that  $S = B_\phi(0)a^2\eta^{-1}R^{-1}\sqrt{\mu_0/mn} = 2.35 \times 10^6$  and  $\text{Pm} = \mu_0\nu/\eta = 0.1$ , where  $\nu$  is the coefficient for isotropic viscous stress ( $\underline{\Pi} = -\nu mn \underline{\mathbf{W}}$ ). The scales for two-fluid effects are  $d_i = 0.22a$ ,  $d_e = 0.005a$ , and  $\rho_s = 0.14a$ .

Our simulation results show that the increase in exponentiation rate of kinetic energy predicted in simplified geometry also occurs in toroidal geometry. Figure 9 shows this nonlinear growth rate as a function of time for two simulations. The transition from current-sheet to ‘X-point’ reconnection is evident from the current density contour plots of Fig. 10. Both simulations use spectral elements with basis functions of polynomial degree eight. The lower resolution computation has a packed  $20 \times 20$  mesh with toroidal Fourier harmonics  $0 \leq n \leq 42$ , and the higher resolution computation has a packed  $24 \times 32$  mesh with  $0 \leq n \leq 85$ . The higher resolution computation uses a more restrictive time-step control as the configuration loses toroidal symmetry, and this is the primary difference between the evolutions shown in Fig. 9. We have subsequently found that the two-dimensional nature of the semi-implicit operator in the flow-velocity advance is the primary cause of the error at larger- $\Delta t$ .

## 5. DISCUSSION AND CONCLUSIONS

The plane-wave analysis of Sect. 3 establishes the most important properties of the staggered implicit algorithm for solving initial-value problems with two-fluid plasma models. First, temporally centered implicit advection in the advance of each field is compatible with the semi-implicit operator for MHD waves in that numerical stability can be achieved without condition on time-step. Second, the Hall electric field and gyroviscosity are also compatible as implicit terms that are centered in the magnetic-field and flow-velocity advances, respectively. Third, implicit resistive dissipation with centered or backward differencing does not adversely affect numerical stability. Fourth, in the absence of physical dissipation, the algorithm does not introduce numerical dissipation. This is important for simulating high-temperature plasma, where physical dissipation, such as electrical resistivity, is small but important for multi-scale phenomena like magnetic reconnection.

Differential approximation supports the major findings of von Neumann analysis and explains the unexpected result that implicit advection with backward differencing is numerically unstable with the staggered algorithm. Our approximation uses the approach of Ref. [26] in dropping terms that require additional initial conditions, but we find it useful to expand different

equations about different times by including synchronization effects in terms that couple the equations. The numerical requirement for stability is apparent from a change of variables for a simplified system that describes two waves propagating with respect to flow. The first differential approximation shows that one of the two equations is ill-posed for forward differencing of advection and the other is ill-posed for backward differencing if the flow speed is less than the wave propagation speed. Compatibility of the semi-implicit operator for MHD with centered advection, Hall term, and gyroviscosity is shown from wave equations for relevant systems. The spatial differential operator acting on the highest temporal derivative is positive for all  $\Delta t$ -values, provided the familiar condition of  $C_0 \geq 1/4$  on the coefficient of the semi-implicit operator.

With physical dissipation terms temporally centered, the algorithm has second-order consistency. Numerical evaluation for plane waves of the two-fluid model shows that the overall accuracy of the implicit leapfrog at large  $\Delta t$ -values is comparable to that of the Crank-Nicolson method for all plane waves except the slow parallel mode that is affected by the ion cyclotron resonance. Here, we see the influence of temporal splitting that is described in Ref. [36]. This particular effect is acceptable for magnetic confinement and other applications where instabilities are most sensitive to distortions that are nearly perpendicular to the magnetic field. Moreover, ion kinetic effects that are not included in the fluid model strongly influence these parallel modes at large wavenumber.

The tearing-mode tests of Sect. 3.1 provide a more realistic confirmation by converging at  $\Delta t$ -values that are typical for semi-implicit MHD accuracy and by reproducing MHD to two-fluid transitions predicted by analytical theory. Accuracy of approximately 1% in the growth rate for non-ideal modes requires  $\Delta t \approx 0.03\gamma^{-1}$ , likely due to distortion of the flow velocity from the semi-implicit operator at larger  $\Delta t$ -values. This stabilizing term is based on the linear ideal-MHD force operator, as in Refs. [16-17], and is self-adjoint. In comparison, the Crank-Nicolson method balance all terms [36] and has comparable accuracy with  $\Delta t$  approximately an order of magnitude larger. The computational cost, however, is a larger and more ill-conditioned matrix that must be solved to advance the system for linear computations or to complete each iteration for a nonlinear computation.

Finally, we note that the NIMROD implementation of the algorithm has been successfully applied to linear two-fluid interchange with gyroviscosity [42] and to two-dimensional nonlinear modeling of magnetic reconnection [43] and spontaneous rotation in the field-reversed configuration [44]. Recent improvements to preconditioning and parallel scaling have improved computational efficiency for nonlinear three-dimensional applications, such as the internal kink mode of Sect. 3.2. Ongoing development includes a semi-implicit operator where the ideal-MHD force operator is based on time-dependent three-dimensional fields to alleviate the dominant accuracy limitations on time-step found from the nonlinear computations.

#### ACKNOWLEDGEMENTS

The authors would like to recognize valuable discussions with and contributions from Daniel Barnes, Dalton Schnack, Richard Nebel, Zoran Mikic, Vladimir Mirnov, Jesus Ramos, Nicholas Murphy, Eric Howell, and Ping Zhu. This work is supported by the U.S. Dept. of Energy through grant FE-FC02-08ER54975 as part of the Center for Extended Magnetohydrodynamics.

Our computations used resources of the National Energy Scientific Computing Center, which is supported by the U.S. Dept. of Energy under Contract No. DE-AC02-05CH11231.

## APPENDIX A. PREDICTOR-CORRECTOR HALL ADVANCE

Reference [19] proposes a self-adjoint fourth-order spatial differential operator for the magnetic-field advance of the Hall-MHD system, instead of making the Hall term time-centered. Expressing Eqs. (8-9) of Ref. [19], which consider the ideal  $\beta \rightarrow 0$  limit with uniform and constant number density, in our dimensionless form, we have

$$\left(1 - \Delta t^2 C_A^2 \nabla^2\right) \Delta \mathbf{V} = \Delta t \mathbf{J}^{j+1/2} \times \mathbf{B}^{j+1/2} \quad (\text{A1})$$

$$\left(1 + \Delta t^2 (\mathbf{C}_H \cdot \nabla)^2 \nabla^2\right) \Delta \mathbf{B} = \Delta t \nabla \times \left(\mathbf{V}^{j+1/2} \times \mathbf{B}^{j+1/2} - \mathbf{J}^{j+1/2} \times \mathbf{B}^{j+1/2}\right) \quad (\text{A2})$$

where both fields are defined at integer time levels, e.g.  $\Delta \mathbf{V} = \mathbf{V}^{j+1} - \mathbf{V}^j$ . The fourth-order differential operator on the left side of (A2) is self-adjoint for solenoidal  $\mathbf{C}_H$ , and it serves as a semi-implicit operator for whistler waves.

The analysis in [19] uses uniform equilibrium magnetic field in the  $z$ -direction, no equilibrium flow, spatial variations of the form  $e^{ikz}$ , and  $\mathbf{C}_H = C_H \hat{\mathbf{z}}$ . It does not provide a definition for the half time-levels appearing on the right sides of (A1-A2).<sup>2</sup> If we set

$$\left(\frac{\underline{v}}{\underline{b}}\right)^{j+1/2} = \lambda^{1/2} \left(\frac{\underline{v}}{\underline{b}}\right)^j \quad (\text{A3})$$

for the  $x$ - and  $y$ -components of the two fields, the eigenvectors satisfy

$$(\lambda - 1) \left(1 + C_A^2 k^2 \Delta t^2\right) \underline{v} = \lambda^{1/2} ik \Delta t \underline{b} \quad (\text{A4})$$

$$(\lambda - 1) \left(1 + C_H^2 k^4 \Delta t^2\right) \underline{b} = \lambda^{1/2} k \Delta t \left[ i \underline{v} + \begin{pmatrix} 0 & -k \\ k & 0 \end{pmatrix} \underline{b} \right]. \quad (\text{A5})$$

Dividing (A4-A5) by  $i \lambda^{1/2}$  and relating the time-step eigenvalue to a frequency through  $\lambda = e^{i\omega \Delta t}$  reproduces Eqs. (10-13) of Ref. [19]. The resulting dispersion relation determines the values of  $C_A$  and  $C_H$  needed for numerical stability. While (A3) holds for analytical waves, it is not consistent with numerical methods such as Crank-Nicolson or predictor-corrector.

If a numerically stable advance can be obtained with a self-adjoint semi-implicit operator for the Hall term, an implementation may use solvers for symmetric matrices, depending on the spatial representation. We therefore consider an algorithm with the staggering described in Sect. 2 and predictor-corrector steps for the Hall advance:

$$\left(1 - \Delta t^2 \mathbf{L}\right) \Delta \mathbf{V} = \Delta t \mathbf{J}^{j+1/2} \times \mathbf{B}^{j+1/2} \quad (\text{A6})$$

<sup>2</sup> The ‘split method’ of Ref. [19] is also not fully specified.

$$\begin{aligned} \Delta \mathbf{B}^* + \Delta t^2 C_{hp} \nabla \times \left\{ \left[ \nabla \times \nabla \times \left( \mathbf{B}^{j+1/2} \times \nabla \times \Delta \mathbf{B}^* \right) \right] \times \mathbf{B}^{j+1/2} \right\} \\ = f_h \Delta t \nabla \times \left( \mathbf{V}^{j+1} \times \mathbf{B}^{j+1/2} - \mathbf{J}^{j+1/2} \times \mathbf{B}^{j+1/2} \right) \end{aligned} \quad (\text{A7})$$

$$\begin{aligned} \Delta \mathbf{B} + \Delta t^2 C_h \nabla \times \left\{ \left[ \nabla \times \nabla \times \left( \mathbf{B}^{j+1/2} \times \nabla \times \Delta \mathbf{B} \right) \right] \times \mathbf{B}^{j+1/2} \right\} \\ = \Delta t \nabla \times \left( \mathbf{V}^{j+1} \times \mathbf{B}^{j+1/2} - \mathbf{J}^* \times \mathbf{B}^{j+1/2} \right) \end{aligned} \quad (\text{A8})$$

where  $\Delta \mathbf{B}^* = \mathbf{B}^* - \mathbf{B}^{j+1/2}$ ,  $C_{hp}$  and  $C_h$  are coefficients for the semi-implicit operator for the Hall term in the predictor and corrector steps, and  $f_h$  controls the centering of the predicted field. When applied to electron-MHD ( $\mathbf{V} = 0$ ) without equilibrium electron flow, the time-step eigenvalues are

$$\lambda = 1 + \left( \frac{1}{1 + C_h \chi^2} \right) \left( \pm i \chi - \frac{f_h \chi^2}{1 + C_{hp} \chi^2} \right), \quad (\text{A9})$$

where  $\chi = ck^2 \Delta t$ . With  $f_h = 1/2$  and  $C_{hp} = C_h/4$ , for example,  $|\lambda| \leq 1$  for  $C_h \geq 1/3$  for all  $\Delta t$ -values. Numerical evaluation of eigenvalues for the Hall-MHD system (A6-A8) with these parameters and  $C_0 \geq 1/4$  finds unstable modes (without equilibrium flows). Another possibility is to use the semi-implicit operator for the Hall term in the corrector step only, i.e.  $C_{hp} = 0$ . The electron-MHD advance is then stable and free of dissipation with  $f_h = 1/2$  and  $C_h = 1/4$ . The algorithm is also stable for the Hall-MHD system. Unfortunately, predictor-corrector advection for equilibrium electron flow requires  $f_h > 1/2$  for conditional stability, but  $f_h > 1/2$  leads to numerical instability for this Hall-MHD advance with or without electron flow.

## APPENDIX B. DIFFERENTIAL APPROXIMATION FOR EXPLICIT LEAPFROG

Our use of differential approximation in Sect. 3.2 provides insight on why numerical instabilities appear with the implicit leapfrog algorithm for certain choices of centering parameters. However, we have not used the standard  $II$ -form that is used to judge stability in Ref. [25]. In this Appendix, we find the  $II$ -form of the differential approximation for a basic explicit leapfrog to find the same necessary conditions for stability that motivate a semi-implicit approach. We consider an algorithm that is consistent of  $O(\Delta t)$ :

$$\frac{v^{j+1} - v^j}{\Delta t} = -\frac{\partial p^j}{\partial y} \quad (\text{B1})$$

$$\frac{p^{j+1} - p^j}{\Delta t} = -\frac{\partial v^{j+1}}{\partial y} . \quad (\text{B2})$$

The first differential approximation from expanding (B1, B2) about time-level  $j$  is the system

$$\frac{\partial v}{\partial t} + \frac{\Delta t}{2} \frac{\partial^2 v}{\partial t^2} = -\frac{\partial p}{\partial y} \quad (\text{B3})$$

$$\frac{\partial p}{\partial t} + \frac{\Delta t}{2} \frac{\partial^2 p}{\partial t^2} = -\frac{\partial v}{\partial y} - \Delta t \frac{\partial^2 v}{\partial y \partial t} . \quad (\text{B4})$$

The form of (B3, B4) with errors from temporal differencing left as derivatives with respect to time is considered the  $I$ -form. Manipulating to eliminate temporal derivatives in terms of spatial derivatives and dropping terms of higher order produces the  $II$ -form of the first approximation:

$$\frac{\partial v}{\partial t} = -\frac{\partial p}{\partial y} - \frac{\Delta t}{2} \frac{\partial^2 v}{\partial y^2} \quad (\text{B5})$$

$$\frac{\partial p}{\partial t} = -\frac{\partial v}{\partial y} + \frac{\Delta t}{2} \frac{\partial^2 p}{\partial y^2} . \quad (\text{B6})$$

For solutions of the form  $e^{iky-i\omega t}$ , the dispersion relation for this system has real eigenvalues  $\omega$  for  $k\Delta t \leq 2$ . This conditional stability for some maximum wavenumber  $k_m$  on a numerical mesh is also found from Eq. (32), where the analysis uses synchronization for the temporally staggered equations. Setting flow and resistive dissipation to zero in Eq. (32) reproduces (B5-B6) with  $p \rightarrow b$ . In fact, the first-order in  $\Delta t$  explicit leapfrog (B1, B2) differs from a second-order version only by the definitions of temporal staggering. Thus, numerical stability criteria must be the same. However, the  $II$ -form of the staggered scheme has no low-order even spatial derivatives when both fields are expanded about the same time and does not reveal a useful stability condition.

## REFERENCES

1. R. D. Hazeltine and J. D. Meiss, Plasma confinement, Addison-Wesley, Redwood City, CA, 1992, pp. 108-113, 194-228.
2. D. Biskamp, E. Schwarz, and J. F. Drake, Two-fluid theory of collisionless magnetic reconnection, *Phys. Plasmas* 4 (1997) 1002-1009.
3. V. V. Mirnov, C. C. Hegna, and S. C. Prager, Two-fluid tearing instability in force-free magnetic configuration, *Phys Plasmas* 11 (2004) 4468-4482.
4. J. F. Drake, M. A. Shay, and M. Swisdak, The Hall fields and fast magnetic reconnection, *Phys. Plasmas* 15 (2008) 42306 1-10.
5. D. G. Swanson, Plasma Waves, 2nd ed., Institute of Physics, Bristol, 2003, pp. 87-103.
6. D. D. Schnack, D. C. Barnes, C. C. Hegna, E. D. Held, C. C. Kim, S. E. Kruger, A. Y. Pankin, and C. R. Sovinec, Computational modeling of fully ionized plasmas using the fluid approximation, *Phys. Plasmas* 13 (2006) 58103 1-21.
7. L. Chacón and D. A. Knoll, A 2D high- $\beta$  Hall MHD implicit nonlinear solver, *J. Comput. Phys.* 188 (2003) 573-592.
8. S. C. Jardin, J. Breslau, N. Ferraro, A high-order implicit finite element method for integrating the two-fluid magnetohydrodynamic equations in two dimensions, *J. Comput. Phys.* 226 (2007) 2146-2174.
9. N. F. Loureiro and G. W. Hammett, An iterative semi-implicit scheme with robust damping, *J. Comput. Phys.* 227 (2008) 4518-4542.
10. O. Czarny and Guido Huysmans, Bézier surfaces and finite elements for MHD simulations, *J. Comput. Phys.* 227 (2008) 7423-7445.
11. J. Crank and P. Nicolson, A practical method for numerical evaluation of solutions of partial differential equations of the heat conduction type, *Proc. Camb. Phil. Soc.* 43 (1947) 50-67.
12. D. R. Reynolds, R. Samtaney, and C. S. Woodward, A fully implicit numerical method for single-fluid resistive magnetohydrodynamics, *J. Comput. Phys.* 219 (2006) 144-162.
13. D. A. Knoll and D. E. Keyes, Jacobian-free Newton-Krylov methods: a survey of approaches and applications, *J. Comput. Phys.* 193 (2004) 357-397.
14. L. Chacón, An optimal parallel, fully implicit Newton-Krylov solver for three-dimensional viscoresistive magnetohydrodynamics, *Phys. Plasmas* 15 (2008) 56103 1-12.
15. D. D. Schnack, D. C. Barnes, Z. Mikic, Douglas S. Harned, and E. J. Caramana, Semi-implicit magnetohydrodynamic calculations, *J. Comput. Phys.* 70 (1987) 330-354.
16. K. Lerbinger and J.F. Luciani, A new semi-implicit method for MHD computations, *J. Comput. Phys.* 97 (1991) 444-459.
17. C. R. Sovinec, A. H. Glasser, T. A. Gianakon, D. C. Barnes, R. A. Nebel, S. E. Kruger, D. D. Schnack, S. J. Plimpton, A. Tarditi, M. S. Chu, and the NIMROD Team, Nonlinear magnetohydrodynamics simulation using high-order finite elements, *J. Comput. Phys.* 195 (2004) 355-386.
18. H. Lütjens and J.-F. Luciani, The XTOR code for nonlinear 3D simulations of MHD instabilities in tokamak plasmas, *J. Comput. Phys.* 227 (2008) 6944-6966.
19. D. S. Harned and Z. Mikic, Accurate semi-implicit treatment of the Hall effect in magnetohydrodynamic computations, *J. Comput. Phys.* 83 (1989) 1-15.
20. C. R. Sovinec, D. D. Schnack, A. Y. Pankin, D. P. Brennan, H. Tian, D. C. Barnes, S. E. Kruger, E. D. Held, C. C. Kim, X. S. Li, D. K. Kaushek, S. C. Jardin, and the NIMROD

- Team, Nonlinear extended magnetohydrodynamics simulation using high-order finite elements, *J. Phys.: Conf. Series* 16 (2005) 25-34.
21. D. Potter, *Computational physics*, Wiley, London, 1973, pp. 65-67.
  22. J. M. Sanz-Serna, Studies in numerical nonlinear instability I. Why do leapfrog schemes go unstable?, *SIAM J. Sci. Stat. Comput.* 6 (1985) 923-938.
  23. L. F. Shampine, Stability of the leapfrog/midpoint method, *Applied Math. and Comput.* 208 (2009) 293-298.
  24. C. W. Hirt, Heuristic stability theory for finite-difference equations, *J. Comput. Phys.* 2 (1968) 339-355.
  25. Y. I. Shokin, *The method of differential approximation*, Springer-Verlag, Berlin, 1983.
  26. E. J. Caramana, Derivation of implicit difference schemes by the method of differential approximation, *J. Comput. Phys.* 96 (1991) 484-493.
  27. R. F. Warming and B. J. Hyett, The modified equation approach to the stability and accuracy analysis of finite-difference methods, *J. Comput. Phys.* 14 (1974) 159-179.
  28. S.-C. Chang, A critical analysis of the modified equation technique of Warming and Hyett, *J. Comput. Phys.* 86 (1990) 107-126.
  29. S. I. Braginskii, Transport processes in a plasma, *Reviews of Plasma Physics* 1, M. A. Leontovich (ed.), Consultants Bureau, New York, 1965, pp. 205-311.
  30. A. N. Simakov and P. J. Catto, Drift-ordered fluid equations for field-aligned modes in low- $\beta$  collisional plasma with equilibrium pressure pedestals, *Phys. Plasmas* 10 (2003) 4744-4757.
  31. Y. Saad, *Iterative methods for sparse linear systems*, 2nd ed., SIAM, Philadelphia, 2003, 164-185.
  32. X. S. Li and J. W. Demmel, SuperLU\_DIST: a scalable distributed-memory sparse direct solver for unsymmetric linear systems, *ACM Trans. Math. Software* 29 (2003) 110-140.
  33. M. O. Deville, P. F. Fischer, and E. H. Mund, *High-order methods for incompressible fluid flow*, Cambridge University Press, Cambridge, 2002, pp. 62-67.
  34. R. Lionello, Z. Mikic, and J. A. Linker, Stability of algorithms for waves with large flows, *J. Comput. Phys.* 152 (1999) 346-358.
  35. <http://www.netlib.org/lapack/index.html>
  36. D. A. Knoll, L. Chacón, L. G. Margolin, and V. A. Mousseau, On balanced approximations for time integration of multiple time scale systems, *J. Comput. Phys.* 185 (2003) 583-611.
  37. B. N. Rogers, R. E. Denton, J. F. Drake, and M. A. Shay, Role of dispersive waves in collisionless magnetic reconnection, *Phys. Rev. Lett.* 87 (2001) 19504 1-4.
  38. E. Ahedo and J. J. Ramos, Parametric analysis of the two-fluid tearing instability, *Plasma Phys. Control. Fusion* 51 (2009) 55018 1-22.
  39. S. V. Bulanov, F. Pegoraro, and A. S. Sakharov, Magnetic reconnection in electron magnetohydrodynamics, *Phys. Fluids B* 4 (1992) 2499-2508.
  40. A. Y. Aydemir, Nonlinear studies of  $m=1$  modes in high-temperature plasmas, *Phys. Fluids B* 4 (1992) 3469-3472.
  41. K. Germaschewski, Nonlinear evolution of the cylindrical tearing mode and its diamagnetic stabilization, *Bull. Am. Phys. Soc.* 53, No. 14 (2008) 80, G11 4.
  42. P. Zhu, D. D. Schnack, F. Ebrahimi, E. G. Zweibel, M. Suzuki, C. C. Hegna, and C. R. Sovinec, Absence of complete finite-Larmor-radius stabilization in extended MHD, *Phys. Rev. Lett.* 101 (2008) 085005 1-4.
  43. N. A. Murphy and C. R. Sovinec, Global axisymmetric simulations of two-fluid reconnection in an experimentally relevant geometry, *Phys. Plasmas* 15 (2008) 042313 1-16.

44. A. I. D. Macnab, R. D. Milroy, C. C. Kim, and C. R. Sovinec, Hall magneto-hydrodynamics simulations of end-shortening induced rotation in field-reversed configurations,” *Phys. Plasmas* 14 (2007) 092503 1-6.

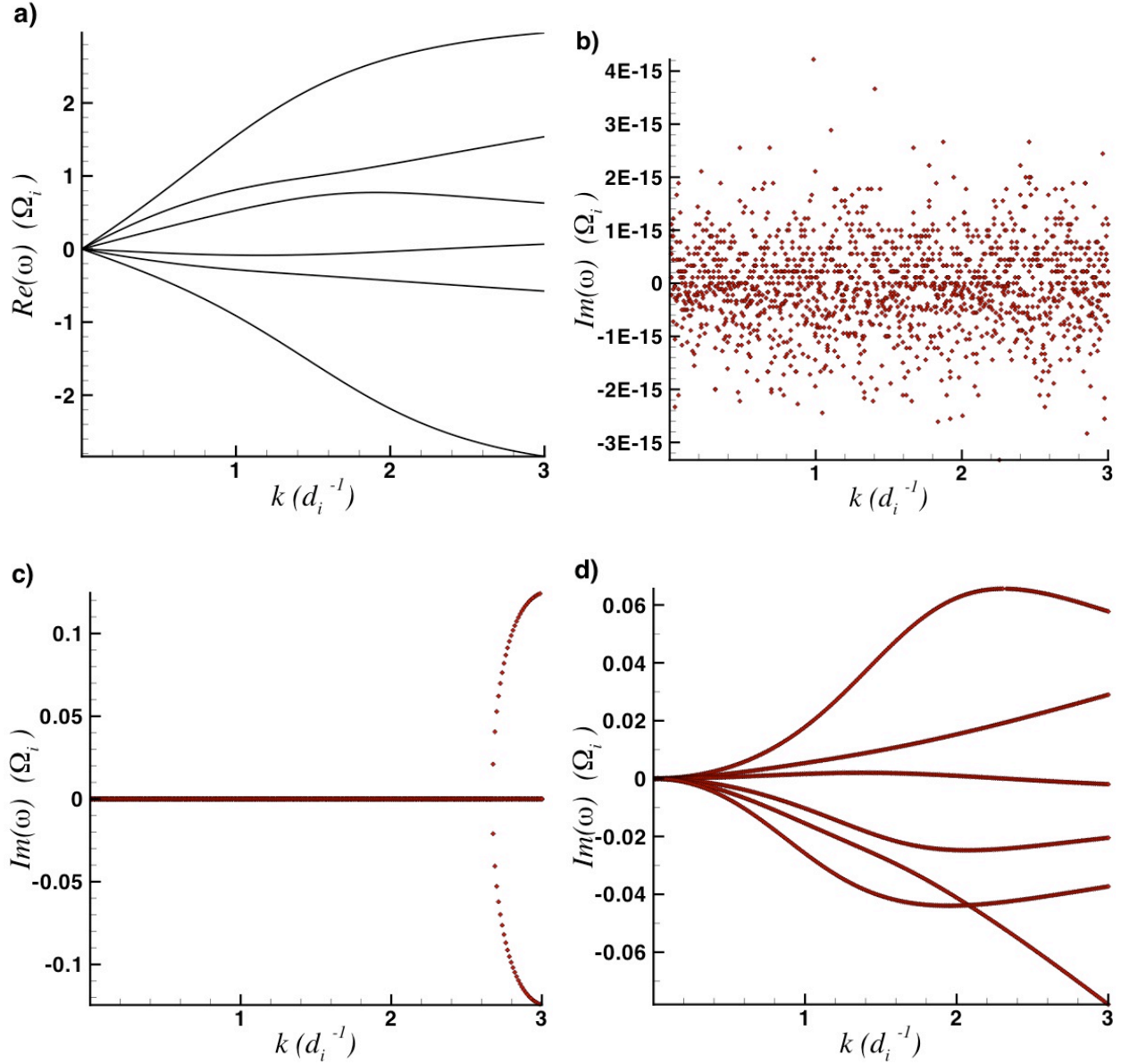


Figure 1. Numerical results from the full dispersion relation for  $\hat{\mathbf{k}} \cdot \hat{\mathbf{b}} = \sqrt{2}/2$ ,  $V_0 = 0.2$ ,  $V_{e0} = -0.3$ , and  $D_\eta = 0$ : a) real and b) imaginary parts of the predicted  $\omega$  for  $\theta = 1/2$  and  $C_0 = 1/4$ , c)  $\text{Im}(\omega)$  for  $\theta = 1/2$  and  $C_0 = 1/8$ , and d)  $\text{Im}(\omega)$  for  $\theta = 3/5$  and  $C_0 = 1/4$ .

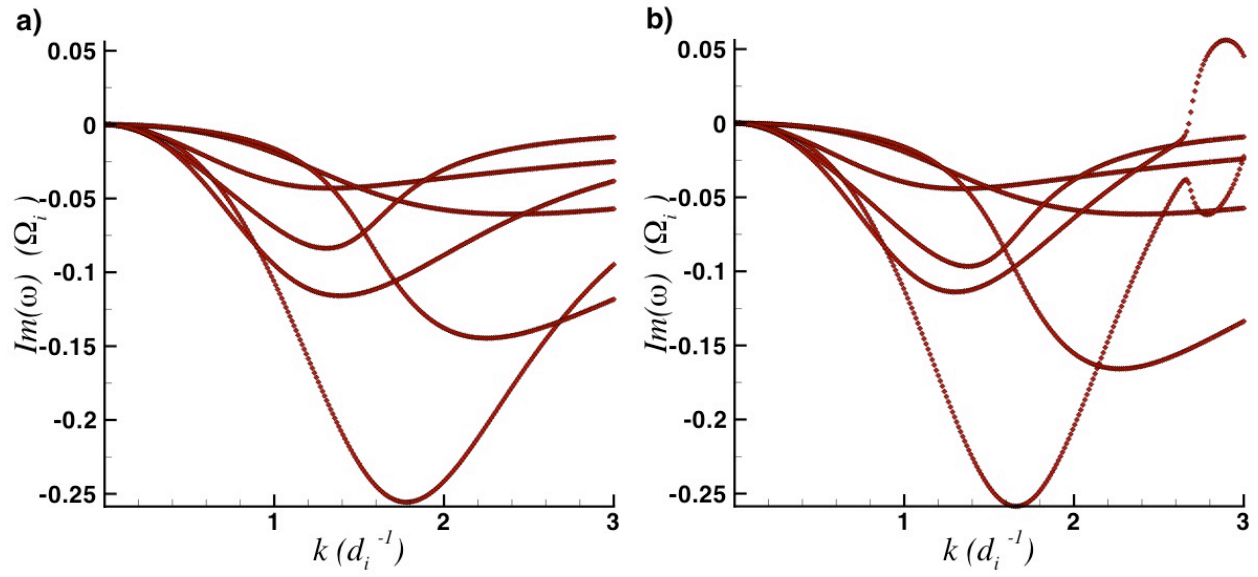


Figure 2. Dispersion relation results for  $\hat{\mathbf{k}} \cdot \hat{\mathbf{b}} = 1/2$  and  $V_0 = 0.2$ ,  $V_{e0} = -0.3$ , and  $D_\eta = 0.2$ : a)  $\text{Im}(\omega)$  for  $\theta_\eta = 1/2$  and b)  $\text{Im}(\omega)$  for  $\theta_\eta = 1/4$ . Advection is centered and  $C_0 = 1/4$ .

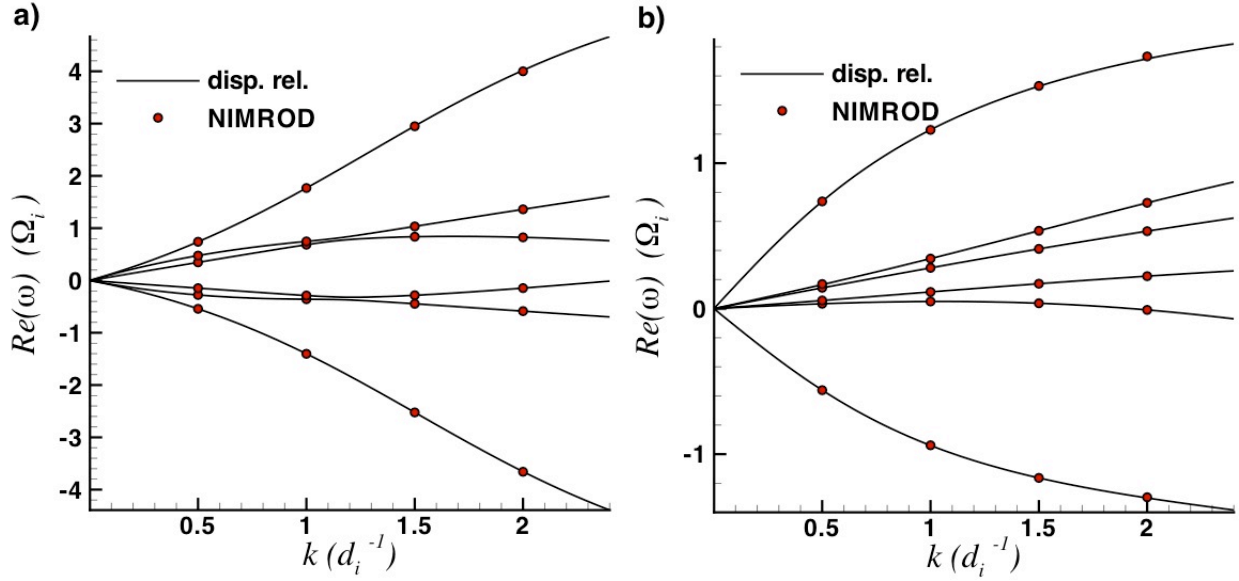


Figure 3. Frequencies from numerical eigenvalues of the full time-step matrix and from NIMROD computations with  $C_0 = 1/4$ ,  $f_e = 1/2$  and centered advection for  $V_0 = 0.2$ . Plots show computations for a) nearly parallel propagation ( $\hat{\mathbf{k}} \cdot \hat{\mathbf{b}} = 0.992$ ) with  $\beta = 0.15$  and  $\Delta t = 0.5$ , and for b) nearly perpendicular propagation ( $\hat{\mathbf{k}} \cdot \hat{\mathbf{b}} = 0.125$ ) with  $\beta = 0.6$  and  $\Delta t = 1.5$ .

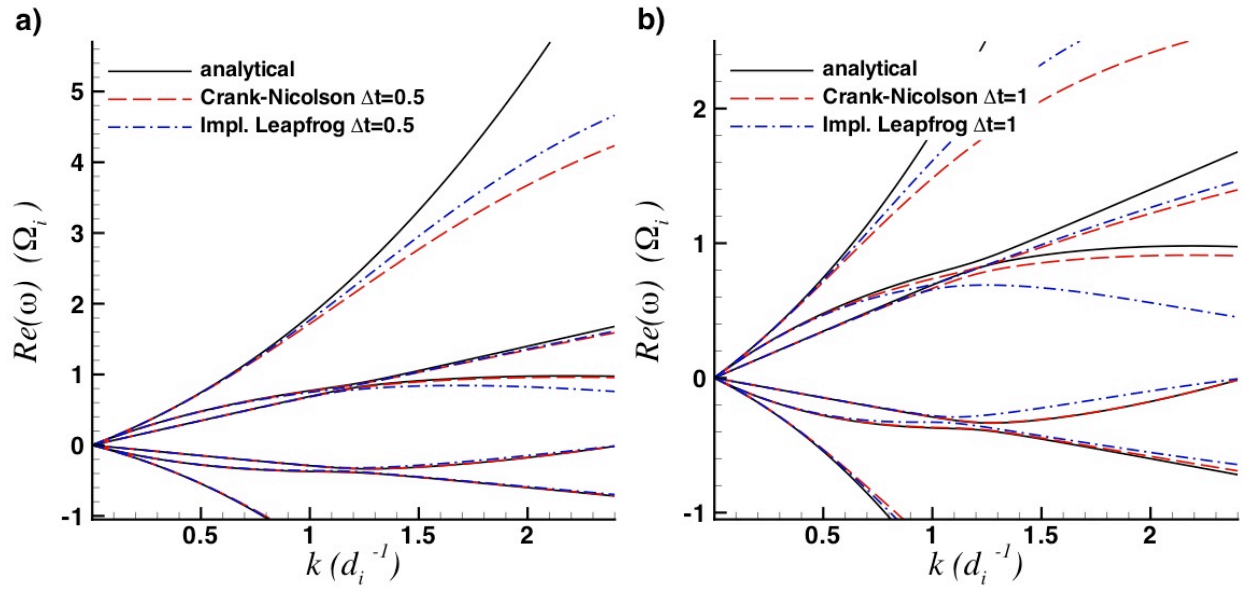


Figure 4. Comparison of frequencies for nearly parallel propagation with a)  $\Delta t = 0.5$  and b)  $\Delta t = 1$  with other parameters as used for Fig. 3a. The three curves display the frequencies from analytical theory and for the Crank-Nicholson and implicit leapfrog methods.

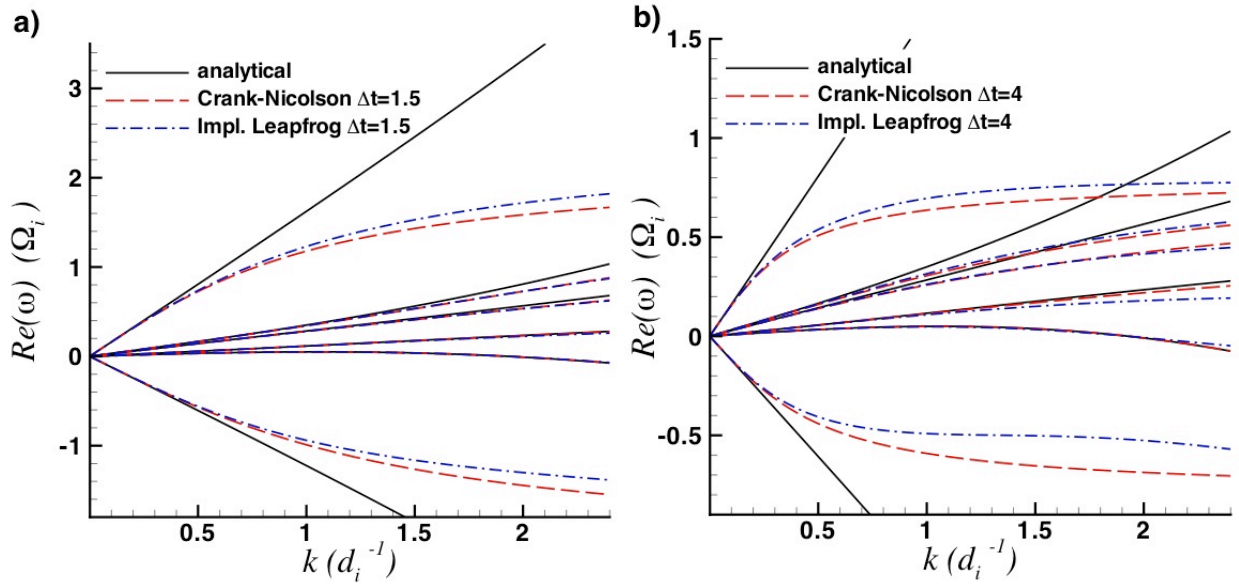


Figure 5. Comparison of frequencies for nearly perpendicular propagation with a)  $\Delta t = 1.5$  and b)  $\Delta t = 4$  with other parameters as used for Fig. 3b.

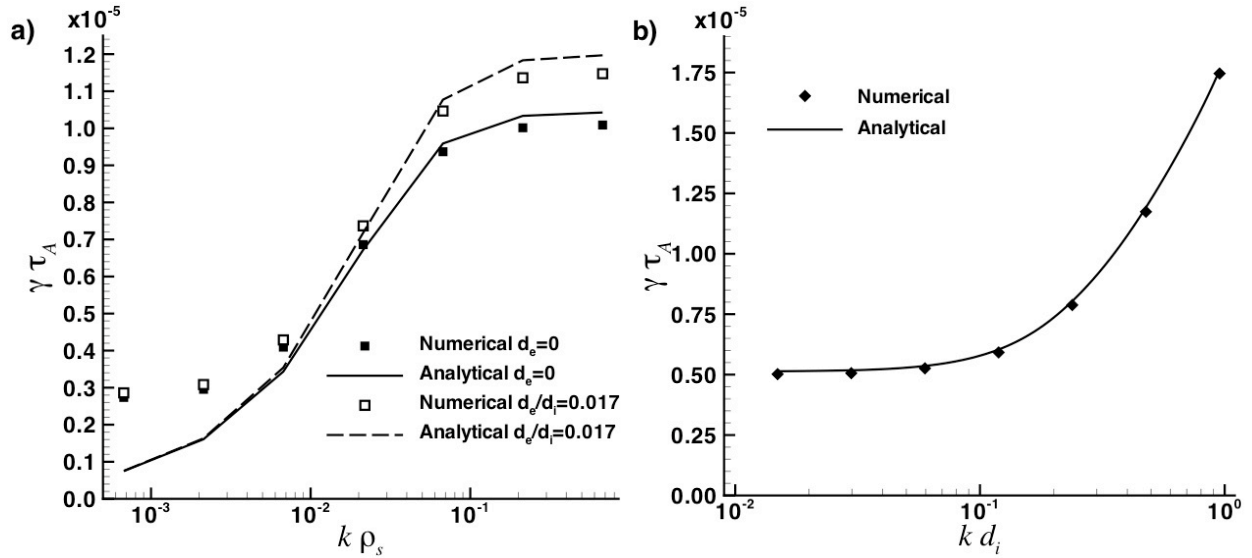


Figure 6. Comparison of numerical tearing-mode growth rates from the NIMROD code with a) theoretical analysis of Ref. [3] for conditions of  $S = 1.79 \times 10^7$ ,  $\Delta'/k = 0.30$ ,  $kL = 0.93$ , and  $k d_i = 2.3$ , and with b) the analysis of Ref. [38] for conditions of  $S = 3.50 \times 10^7$ ,  $\Delta'/k = 1.45$ ,  $kL = 0.76$ , and  $\beta = 0.05$ . Gyroviscosity is not considered in the theory or in the computations. Dimensionless parameters are as defined in the text.

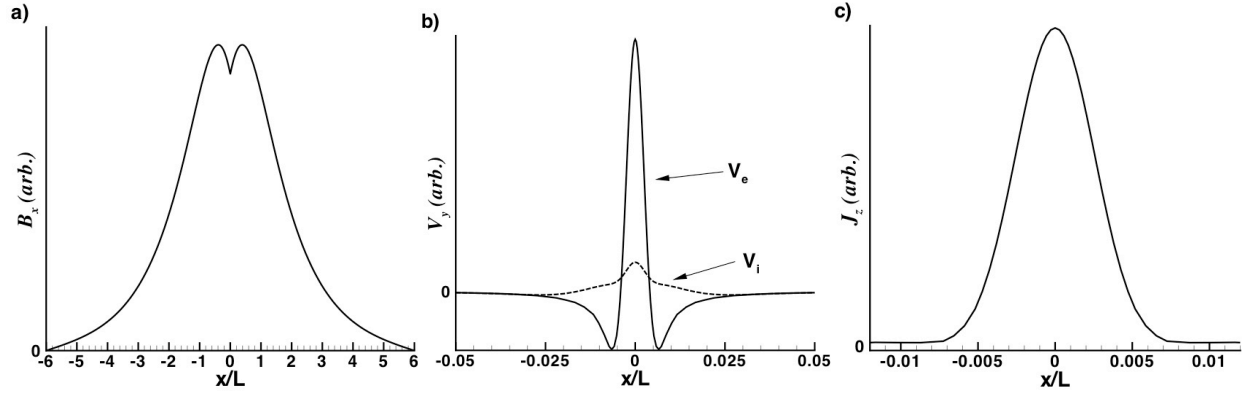


Figure 7. Components of the eigenfunctions from the  $kd_i = 0.238$  computation for comparison with Ref. [38]: a) component of perturbed  $\mathbf{B}$  in the  $x$ -direction, b) component of perturbed ion ( $\mathbf{V}_i \equiv \mathbf{V}$ ) and electron ( $\mathbf{V}_e \equiv \mathbf{V} - \mathbf{J}/ne$ ) velocities perpendicular to the guide field and in phase with  $B_x$ , and c) component of perturbed current density parallel to the guide field and out of phase with  $B_x$ .

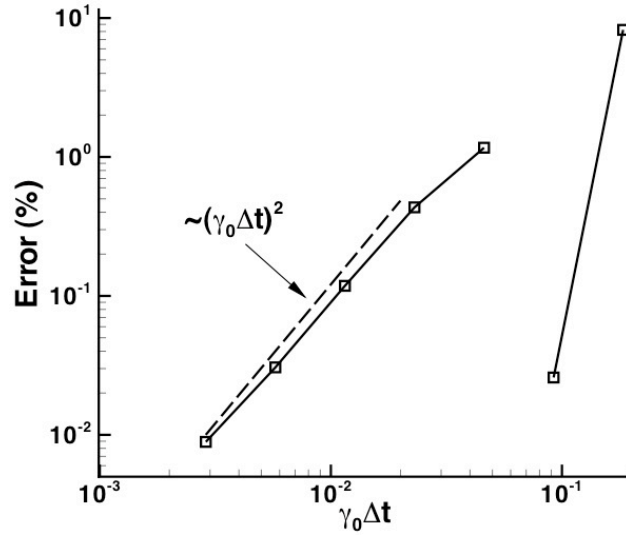


Figure 8. Temporal convergence of the growth rate for the mode shown in Fig. 7. The error is defined as  $|\gamma - \gamma_0|/\gamma_0$ , where the reference value  $\gamma_0$  is computed at  $\gamma_0 \Delta t = 7.19 \times 10^{-4}$ . The break in the curve shows where the error changes sign.

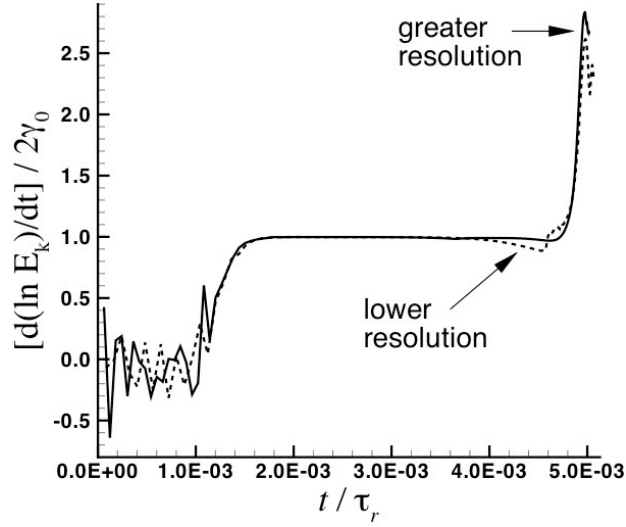


Figure 9. Evolution of the exponentiation rate of kinetic energy, normalized by the linear growth-rate, as a function of time from the two nonlinear computations. The linear growth rate of the internal kink mode is  $\gamma_0 R \sqrt{\mu_0 m n} / B_\phi(0) = 1.90 \times 10^{-3}$  for this equilibrium and parameter set, and the resistive diffusion time is defined as  $\tau_r \equiv \mu_0 a^2 / \eta$ .

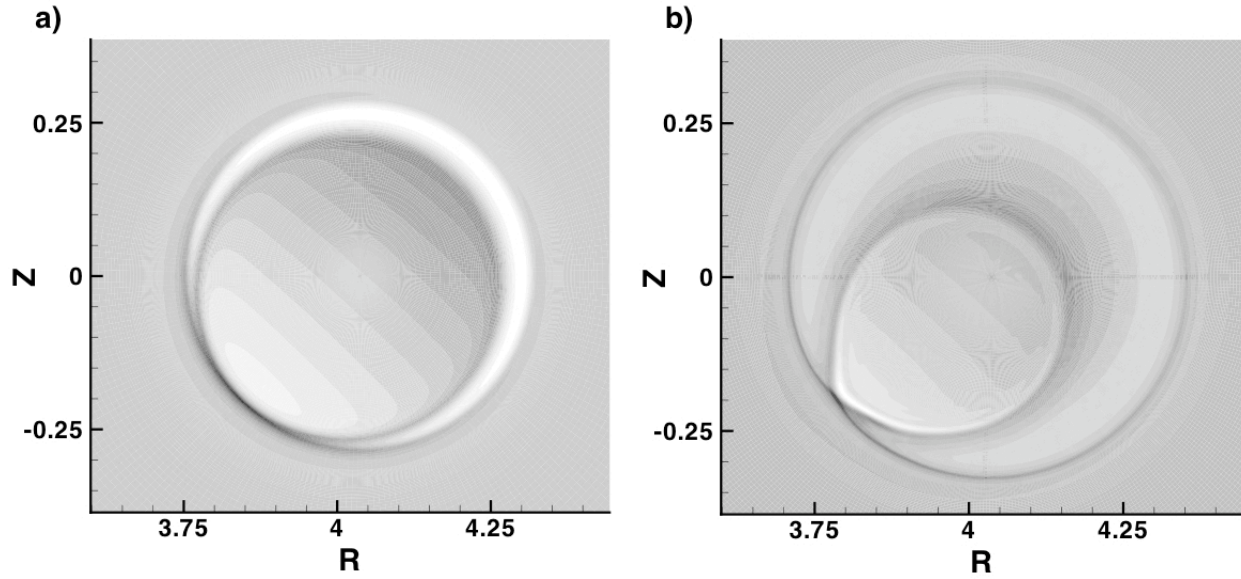


Figure 10. Contours of constant current density parallel to  $\mathbf{B}$  in the vicinity of the resonance and at a plane of fixed toroidal angle a) before the increase in growth rate,  $t = 4.67 \times 10^{-3} \tau_r$ , and b) after the increase,  $t = 4.95 \times 10^{-3} \tau_r$ .